Microstructural Evolution During High-temperature Oxidation of Ti_2AlC ceramics

Bai Cui, Daniel D Jayaseelan, William Edward Lee*

Centre for Advanced Structural Ceramics (CASC) and Department of Materials, Imperial College

London, South Kensington campus, London SW7 2AZ, UK

* Corresponding author. Tel.: +44 (0)20 7594 6733; fax: +44 (0)20 7594 6736; email:

w.e.lee@imperial.ac.uk.

Abstract

Microstructural development during high-temperature oxidation of Ti_2AlC below 1300 ºC involves gradual formation of an outer discontinuous TiO_2 layer and an inner dense and continuous α-Al_2O_3 layer. After heating at 1400 ºC, an outer layer of mixed TiO_2 and Al_2TiO_5 phases and a cracked α-Al_2O_3 inner layer were formed. After heating to 1200 ºC and cooling to room temperature, two types of planar defect were identified in surface TiO_2 grains: twins with (2 0 0) twin plane and stacking faults bounded by partial dislocations. Formation of planar defects released thermal stresses that had generated in TiO_2 grains and arise from thermal expansion mismatch of the phases (TiO_2, α-Al_2O_3 and Al_2TiO_5) in the oxide scale. After heating to 1400ºC and cooling to room temperature, crack propagation in TiO_2 grains resulted from the thermal expansion mismatch of the phases in the oxide scale, the high anisotropy of thermal expansion in Al_2TiO_5 and the volume changes associated with the reactions during Ti_2AlC oxidation. An atomistic oxidation mechanism is proposed, in which the growth of oxide scale is caused by inward diffusion of O^{2-} and outward diffusion of Al^{3+} and Ti^{4+}. The weakly bound Al leaves the Al atom plane in the layered structure of Ti_2AlC, and diffuses outward to form a protective inner α-Al_2O_3 layer between 1100 and 1300 ºC. However, the α-Al_2O_3 layer becomes cracked at 1400 ºC, providing channels for rapid ingress of oxygen to the body, leading to heavy oxidation.

Keywords

Microstructure; Oxidation; MAX phases

1. Introduction

Ti_2AlC is one of a series of ceramics termed MAX phases. These are a family of ternary compounds with the general formula of $M_{n+1}AX_n$ [1-4] which have properties between those of metals and ceramics [1-3]. Like a metal, Ti_2AlC is readily machinable, thermal-shock resistant, thermally and electrically conductive and damage tolerant; like a ceramic, it is lightweight (4.11 g cm^{-3}), refractory, elastically stiff and oxidation resistant. This unique combination makes Ti_2AlC a promising material for use in diverse fields, especially in high-temperature applications such as electrical heating elements (Maxthal®, made by Kanthal AB) [5], cladding materials in lead-cooled fast breeder nuclear reactors [6], high-temperature electrodes, and catalyst supports for automobiles [4].

The oxidation behaviour of Ti_2AlC (~23 μm average grain size, 4 vol % impurity phases containing O and P) was initially studied by Barsoum *et al.* [7] who observed formation of non-protective oxide scales which are comprised mainly of a rutile-based solid solution $(Ti_{1-y}Al_y)O_{2-y/2}$ where y <0.05 and some Al_2O_3. Later work e.g. Sunderberg *et al.* [5] reported formation of a 15 μm thick protective α- Al_2O_3 layer after 8000 oxidation cycles up to 1350 °C on commercial Ti_2AlC samples (Maxthal®). Zhou *et al.* observed a continuous inner protective α-Al_2O_3 layer and a discontinuous outer layer of TiO_2 up to 1300 °C on Ti_2AlC ceramics (phase-pure dense polycrystalline) [8, 9]. Reasons for these different observations likely include different as-made ceramic microstructures, impurity contents, temperatures, times and atmospheres. Moreover, these results revealed that the oxidation mechanism of Ti_2AlC is not fully understood.

Knowledge of the microstructural evolution of the oxide scale on Ti_2AlC after differing conditions of time, temperature and atmosphere is crucial for a complete understanding of its oxidation mechanism. In the present work, the microstructural evolution of Ti_2AlC ceramic during oxidation in air was investigated from 900-1400 °C.

Generally, the oxidation resistance of high-temperature ceramics and alloys depends on the formation of a protective surface oxide. In an ideal case, the oxide layer is highly stable, slow growing, free from pores or cracks, adherent and coherent [10]. In many cases, α-Al_2O_3 provides an oxide which comes close to satisfying these requirements. The slow growth rate is related to its

highly stoichiometric structure and the low diffusion coefficients of Al^{3+} and O^{2-} in α-Al_2O_3. In the final part of this paper, an atomistic mechanism involved in growth of the oxide scale on Ti_2AlC is discussed.

2. Experimental

Ti_2AlC samples were prepared by uniaxial hot-pressing Ti, Al and graphite starting materials at 1400 °C for 1h at 30 MPa in flowing Ar and were supplied by Prof. Yanchun Zhou (Shenyang National Laboratory for Materials Science, Chinese Academy of Sciences). More details of sample processing are found in reference [11]. The as-received samples are predominantly single-phase Ti_2AlC ceramics as determined by XRD analysis, with densities of 4.10 g/cm^3 (99.8% theoretical) measured by the Archimedes method. Samples for oxidation experiments were cut by diamond saw to ~ 4×4×4 mm in size. The surfaces were ground down to 1200 grit, polished to 1 μm, followed by degreasing in acetone. Thermogravimetry (TG) experiments were performed in a thermal analyzer (Netzsch STA 449C Jupiter, Netzsch Instruments, Aldridge, UK) by heating the Ti_2AlC samples (approximately 3.5×3.5×3.5 mm in size) from ambient temperature to 1200 °C at a rate of 10 and 20 °C min^{-1} in a flowing air atmosphere. The samples used for TG were the same as those for oxidation tests (only smaller in size to fit into the α-Al_2O_3 crucibles) in order to understand the phase evolution associated with Ti_2AlC oxidation. Differential thermogravimetry (DTG) curves were derived from the TG curves. During oxidation experiments, samples were placed on a Pt crucible and heated to temperature at 20°C/min in an open hearth furnace. Isothermal oxidation runs were performed for 1h from 900-1400 °C in air before samples were removed and air cooled. In addition, both cyclic and isothermal oxidation at 1400 ºC were carried out in a thermal analyzer (Netzsch STA 449F1, Netzsch Instruments, Aldridge, UK) by heating the same sized Ti_2AlC samples (approximately 3.5×3.5×3.5 mm) in a flowing air atmosphere. During the cyclic oxidation experiments, in each cycle the sample was heated to 1400 ºC at 20°C/min, held at 1400 ºC for 1h, before cooling to room temperature at 20°C/min. In total 10 cycles were carried out continuously. During the isothermal oxidation experiments, the sample was heated to 1400 ºC at 20°C/min, held at 1400 ºC for 10h, before cooling to room temperature at 20°C/min.

Microstructures of the oxide scales on the Ti_2AlC samples were characterized *post mortem* at room temperature. Phases present in oxidized samples were characterized using an X-ray diffractometer (Philips PW1700, Eindhoven, The Netherlands) with Cu Kα radiation. Quantitative analysis was carried out by calculating the normalized intensity of the highest diffraction peaks of each phase [12, 13]. The errors of quantitative analysis were determined by repeating calculations 3 times for parallel samples. The surface and cross-section microstructures were investigated using a field emission gun scanning electron microscope (FEGSEM, Gemini LEO 1525, Oberkochen, Germany) operated with secondary electron imaging (SEI), coupled with energy dispersive spectroscopy (EDS) for chemical analysis (Oxford Instruments INCA, Oxford, UK, using an ultra-thin window (UTW) detector which is capable of detecting light elements with atomic number Z>4). Prior to FEGSEM, a thin layer of chromium was sputtered on the surface of the oxidized samples to avoid electron charging, because the electrical conductivity of oxidation products (TiO_2 and Al_2O_3) is low. The crack densities were quantified from the SEI images by a stereological intercept method [14].

100 nm-thick sections for transmission electron microscopy (TEM) were prepared using the *in situ* lift-out technique on a single-beam focused ion beam (FIB) instrument (FEI FIB200, FEI Europe Ltd., Cottenham, UK). An FEI FIB 200 single-beam workstation using a 30 keV gallium liquid metal ion source and a platinum gas injection system was modified and fitted with a Kleindiek piezo-electric micromanipulator to enable specimen lift-out to be performed *in situ* [15, 16]. During FIB section preparation, a Pt protection layer was deposited to protect the feature of interest from Ga^+ milling, and then a cross-section containing the feature of interest was lifted-out and attached to a support grid that fits in a TEM specimen-holder. TEM was carried out with an electron microscope operated at 200 kV (JEM 2000FX, JEOL Ltd., Tokyo, Japan) and a high-resolution electron microscope operated at 200 kV (JEM 2010, JEOL Ltd., Tokyo, Japan). Microstructures were examined in the TEM using bright-field (BF) imaging and dark-field (DF) imaging and selected area electron diffraction (SAED) crystallographic analysis (operated using a double-tilt holder). In addition, EDS chemical analysis in the JEM 2010 was performed using an UTW detector (Oxford Instruments INCA, Oxford, UK).

3. Results and Discussion

3. 1 Phase evolution during Ti_2AlC oxidation

Figure 1 shows XRD after oxidation of Ti_2AlC samples at 900-1400 ºC in air for 1 h. The phase composition of the oxide scale detected via XRD is summarized in Table 1, which reveals TiO_2 (rutile), α-Al_2O_3, and Al_2TiO_5. The intensity of Ti_2AlC diffraction peaks decreases with increasing oxidation temperature, suggesting that Ti_2AlC is oxidized at temperatures from 900 to 1400 ºC. By 900 ºC TiO_2 (rutile) starts to be detected in the oxide scale, but the rutile peak intensity remains nearly constant from 900-1400 ºC (Table 1). α-Al_2O_3 is initially present in the oxide scale after oxidation at 1000 ºC, and α-Al_2O_3 peak intensity increases significantly with temperature.

Al_2TiO_5 forms by reaction between TiO_2 and Al_2O_3 [8, 12, 17]:

$$TiO_2 + Al_2O_3 \longrightarrow Al_2TiO_5 \qquad \Delta V=10.8\%,\ \Delta m=0 \qquad (1)$$

Al_2TiO_5 is present in the oxide scale after heating at 1400 ºC. Together with the presence of Al_2TiO_5, the intensity of diffraction peaks associated with TiO_2 (rutile) after 1400 ºC reveals a small drop compared with that after 1200 ºC, suggesting formation of Al_2TiO_5 consumes some rutile.

TG and the corresponding DTG curves for Ti_2AlC are shown in Figure 2. TG reveals a significant mass increase near 920 ºC (at 10 °C min^{-1}) or 940 ºC (at 20 °C min^{-1}), suggesting significant oxidation products were formed at this temperature. Below this temperature, the sample mass increased slowly. XRD revealed that after oxidation at 900 ºC, the oxidation product is mainly TiO_2 (rutile) (Table 1). Thus, the gradual increase in weight before 920 ºC (at 10 °C min^{-1}) or 940 ºC (at 20 °C min^{-1}) is associated with TiO_2 (rutile) formation. A DTG peak occurred at 999.2 ºC (at 10 °C min^{-1}) or 1009.8 ºC (at 20 °C min^{-1}). XRD revealed that after oxidation at 1000 ºC, α-Al_2O_3 was present in the oxide scale indicating the DTG peak is likely associated with formation of α-Al_2O_3. The formation of α-Al_2O_3 triggers a large mass increase (as shown in Equation 3), which corresponds to the peak in the DTG curve.

Based on the above analysis, oxidation of Ti_2AlC occurs via the reactions:

$$Ti_2AlC + xO_2 \longrightarrow Ti_{2-x}AlC + xTiO_2(rutile),\ x \le 0.051 \qquad (T< 940\ ºC)$$

(2)

$$Ti_2AlC + \frac{15}{4}O_2 \longrightarrow 2TiO_2(rutile) + \frac{1}{2}\alpha - Al_2O_3 + CO_2 \qquad \Delta V=59.0\%,\ \Delta m=56.4\%$$

(T > 940 ºC) (3)

At 1400 ºC, as discussed above (Equation 1), TiO_2 (rutile) and α-Al_2O_3 reacted to form Al_2TiO_5. In reaction 2, the x value was estimated from the TiO_2 (rutile) content in the oxide scale at 900 ºC (Table 1). Clearly, the Gibbs free energies of reactions 2 and 3 depend on the temperature and oxygen partial pressure. In addition, the Gibbs free energy of reaction 3 also depends on the CO_2 partial pressure.

3.2 Microstructural evolution during Ti_2AlC oxidation

To fully understand the microstructural evolution of the oxide scale on Ti_2AlC, both plan view and cross-section samples after oxidation at 1000-1400 ºC were investigated by FEGSEM and EDS.

Typical surface morphologies of the oxide scales formed after oxidation at different temperatures are presented in Figure 3. The surface morphologies and compositions of phases formed on Ti_2AlC changed with temperature. After oxidation at 900 ºC (Figure 3a), small grains (<1 μm) were present on the surface of Ti_2AlC, which EDS indicated were mainly Ti and O presumably present as TiO_{2-x}. Intermediate TiO_{2-x} phases have also been found during low temperature oxidation of Ti [18]. For example, Ti oxidises after heat treatment at 370 ºC through a series of intermediate TiO_{2-x} phases until complete oxidation to rutile TiO_2 occurs at ~500 ºC [18]. After oxidation at 1000 ºC (Figure 3b), large angular surface grains (5-10 μm) were observed which EDS suggests are TiO_2, while the smaller grains (<1 μm) were probably α-Al_2O_3 as indicated by EDS. After oxidation at 1200 and 1300 ºC (Figure 3c and d), large TiO_2 (rutile) grains (5-15 μm) containing planar defects were dispersed throughout the small (<2 μm) angular α-Al_2O_3 grains. The planar defects present in the TiO_2 grains will be discussed later. After oxidation at 1400 ºC (Figure 3e), small nodular grains (~1.2 μm) have developed along the edge of large (5-20 μm) TiO_2 grains. EDS analysis revealed that the Ti/Al atomic ratio is close to 1:2. Supported by the results of phase analysis of samples oxidized at 1400 ºC (Table 1), the small nodular grains are most likely to be Al_2TiO_5. The planar defects on TiO_2 grains, which were present at 1200 and 1300

ºC are no longer present after oxidation at 1400 ºC. In addition, cracks were developed in TiO_2 grains at 1300 and 1400 ºC (Figure 3d and e).

Figures 4-6 show SEI images of cross-sections of Ti_2AlC samples oxidized at 1000, 1200 and 1400 ºC respectively, and the corresponding EDS line-scanning profiles.

After oxidation at 900 ºC, a thin (less than 1 μm) oxide layer formed (not shown). EDS analysis shows that the phase in the oxide scale is TiO_2, consistent with the XRD (Figure 1, Table 1).

After oxidation at 1000 ºC (Figure 4a), over most of the Ti_2AlC surface, a thin (about 1 μm) oxide layer was formed. In addition, thick bumps (1-4 μm thick) are distributed over the oxide scale at intervals of several microns. To investigate the microstructure of the thin oxide layer and the thick bumps, EDS line-scans were made along the black and grey arrows, which cross the thin oxide layer and a thick bump, respectively. EDS line-scanning profiles along the black arrow are shown in Figure 4b. The peaks of Al and O concentrations are clearly observed in the oxide scale, indicating formation of α-Al_2O_3 throughout the oxide scale. Ti concentration decreases from the unoxidised Ti_2AlC side to the oxide scale surface, and a small Ti peak is present near the oxide scale surface, indicating more TiO_2 formed there. The microstructure of the thin layer in Figure 4a is a mixture of TiO_2 and α-Al_2O_3, with more TiO_2 formation near the oxide scale surface. EDS line-scanning profiles along the grey arrow (Figure 4c) which cross the thick bumps, reveal different features. A peak of Al concentration and a peak of Ti concentration are present at the inner and outer parts of the oxide scale, respectively, which suggests that an outer layer of TiO_2 and an inner layer of α-Al_2O_3 are formed on the thick bumps. As will be shown later, such a microstructure is similar to that of the oxide scale on Ti_2AlC at 1200 ºC, implying that the oxidation of Ti_2AlC in thick bumps is enhanced relative to that in the thin layers. This behaviour may be explained by the presence of defects and cracks (induced by polishing) at the positions of the bumps on the original Ti_2AlC surface, which decreased the activation energy for oxidation. In addition, it is interesting to note that the bumps also penetrate into the original Ti_2AlC surface, which will be discussed further later.

After oxidation at 1200 ºC (Figure 5a), a uniform and continuous thick (2-4 μm) oxide scale was formed. EDS line-scanning profiles along the black vertical line are shown in Figure 5b. A peak of Al concentration and a peak of Ti concentration are present in the inner and outer parts of

the oxide scale, respectively, which indicates that the outer layer is TiO_2 and the inner layer is α-Al_2O_3. Clearly, in samples oxidized from 1100 to 1300 ºC, a two-layer microstructure forms.

In samples oxidized at 1400 ºC, the oxide scale grows to 5-10 μm thick and becomes cracked (Figure 6a). EDS analysis (Figure 6b) revealed that Al and O are present throughout, indicating that α-Al_2O_3 is the major phase in the oxide scale. A small Ti peak is present on the outer part of the oxide scale. SEM revealed that the surface of the sample oxidized at 1400 ºC is covered by TiO_2 and Al_2TiO_5 (Figure 3e). Thus, it can be concluded that the oxide scale microstructure after 1400 ºC is cracked α-Al_2O_3 in the inner part, while the outer layer comprises TiO_2 and Al_2TiO_5.

3.3 Planar defects: FIB-TEM investigations

After oxidation at 1200 and 1300 ºC, surface TiO_2 (rutile) grains contain planar defects (Figure 3c and d). FIB sectioning was performed for sample oxidized at 1200 ºC to further understand the nature and formation mechanism of these planar defects. Planar defects were observed, which can be divided into two types: twins and stacking faults.

Figure 7a shows a BF image of TiO_2 twins. The SAED pattern shown in Figure 7b was recorded along the [0 1 1] zone axis and consists of overlapped patterns corresponding to each crystal located on either side of the mirror plane. The twins have tetragonal rutile structure, showing the (2 0 0) mirror planes (= twin planes). (1 0 0), (-1 0 0), (3 0 0), (-3 0 0)…, which are forbidden reflections along the rutile [0 1 1] zone axis, are present due to double diffraction.

Figure 8a, b and d show BF, DF and HRTEM images of stacking faults in TiO_2 grains. Alternating bright and dark fringes are observed and visibility of fringes decreases towards the centre of the fault. The symmetrical nature of the BF image and the asymmetrical nature of the DF image, due to anomalous absorption effects, are clearly visible [19, 20] confirming these are stacking faults. In addition, these stacking faults are bounded by partial dislocations (arrowed in Figure 8b) lying inside the grain.

The formation of planar defects can release large thermal stresses in TiO_2 grains. During oxide scale growth on the Ti_2AlC surface, thermal stresses (arising from thermal expansion coefficient (TEC) mismatch of the phases in the oxide scale) gradually accumulate in TiO_2 grains. The TEC

of these phases are: rutile (α_a= 9.2 ×10^{-6} K^{-1}, α_c= 7.1 ×10^{-6} K^{-1}), α-Al_2O_3 (α_a= 7.9 ×10^{-6} K^{-1}, α_c = 8.8 ×10^{-6} K^{-1}), Al_2TiO_5 (α_a= 10.9 ×10^{-6} K^{-1}, α_b= 20.5 ×10^{-6} K^{-1}, α_c= -2.7 ×10^{-6} K^{-1} [21], 0-1273 K; α_a= 9.8×10^{-6} K^{-1}, α_b= 20.6 ×10^{-6} K^{-1}, α_c= -1.4×10^{-6} K^{-1} [22]), and Ti_2AlC (α_a= (7.1±0.3) ×10^{-6} K^{-1}, α_c= (10±0.5) ×10^{-6} K^{-1}, 297-1573K) [23]. The large TEC anisotropy in Al_2TiO_5 grains is particularly significant. Hasselman assumed that in a solid body constrained in all directions and uniformly cooled through a temperature difference ΔT, the triaxial thermal stress can be given by [24, 25]:

$$\sigma = \frac{\alpha \Delta T E}{1-2\nu} \qquad (4)$$

where α is the average thermal expansion coefficient for the temperature range involved, E is Young's modulus, ν is Poisson's ratio. After oxidation at 1200 and 1300 ºC and cooling to room temperature, planar defects including twins and stacking faults were formed, partly releasing the thermal stresses. After oxidation at 1300 and 1400 ºC and cooling to room temperature, cracks were developed (Figure 3d and e) in TiO_2 grains, which can release additional thermal stress. When the thermal stresses are greater than the strength of rutile TiO_2, they will result in crack propagation and failure of the component. Planar defects were no longer present in TiO_2 grains after heating to 1400 ºC, and they are probably annealed out.

Crack formation after 1400 ºC may have three origins. First, the thermal expansion mismatch of the phases in the oxide scale, which causes the cracks during rapid cooling. Second, the high anisotropy of thermal expansion in Al_2TiO_5 is known to trigger spontaneous microcracking upon cooling when a critical size is exceeded [26, 27]. The Al_2TiO_5 grain size observed is about 1.2 μm (Figure 3e), much larger than the critical size for spontaneous microcracking in Al_2TiO_5 ($d_{crit} = k\frac{G_{c,gb}}{Y(\Delta\alpha\Delta T)^2}$ = 0.4 μm,, where k is a constant, $G_{c,gb}$ is the grain boundary fracture toughness, Y is Young's modulus, $\Delta\alpha$ is the maximum anisotropy of the thermal expansion coefficient, and ΔT is the temperature difference [26, 27]). Third, the volume changes (ΔV) associated with the reactions during Ti_2AlC oxidation are large (see Equation 1 and 3). Stress generated by formation of reaction products with larger volumes than the reactants can cause cracks to form [28].

Figure 9a and b shows the typical surface morphology of Ti_2AlC samples after cyclic oxidation

and isothermal oxidation at 1400 ºC, respectively. Clearly, the sample after cyclic oxidation (Figure 9a) not only has higher crack density (0.0160±0.0012 μm^{-2}), but the small cracks also grew into long cracks. The sample after isothermal oxidation (Figure 9b) has fewer cracks and less crack growth (crack density= 0.0106±0.0008 μm^{-2}). In addition, the sample after cyclic oxidation has more mass gain (about 14.7%) compared with that after isothermal oxidation (about 10.3%). This can be explained by the greater crack density in the sample during cyclic oxidation, providing channels for rapid ingress of oxygen to the body. Oxygen passes through these cracks, and then reacts with Ti_2AlC to form more α-Al_2O_3, TiO_2 and Al_2TiO_5. As a result, the sample after cyclic oxidation has more severe oxidation and more mass gain. The results of the cyclic oxidation experiments indicate that thermal expansion mismatch between the phases present causes cracks to form on cooling. However, the volume changes may also cause cracks. Compared with the sample after isothermal oxidation at 1400 ºC for 1h (Figure 3e, crack density = 0.0082±0.0010 μm^{-2}), the sample after isothermal oxidation at 1400 ºC for 10h (Figure 9b) has greater crack density. The increase of isothermal oxidation time allows more Ti_2AlC to oxidize, generating more oxidation products and thus more stress, causing more cracks to form [28].

In addition to the stress relaxation caused by microcrack formation, creep relaxation [26] might also be occurring. In this study, a number of dislocations were observed by TEM in the oxidized Ti_2AlC samples, and thus dislocation creep [26] might occur. However, the samples were oxidized at 1400 ºC for 1 hour, which is probably too short a time for creep to have much effect.

3.4 Diffusion mechanism of microstructural evolution

Ti_2AlC oxidation kinetics have been measured by various researchers [29-31]. Parabolic oxidation kinetics have been observed, which implies growth of the oxide scale is diffusion-controlled [26, 29-31]. In Ti_2AlC, the oxide scale growth is caused by inward diffusion of O^{2-} and outward diffusion of Al^{3+} and Ti^{4+} [29-31]. Al^{3+} and Ti^{4+} are from Ti_2AlC, and diffuse outward through the oxide scale. O^{2-} is from O_2 in air, and diffuses inward through the oxide scale. In this study, thick bumps which were present in the oxide scale (Figure 4a) provide some indication of the modes of diffusion during oxide scale growth. One side (the oxide scale/substrate

interface) of the bump penetrates into the Ti_2AlC substrate, while the other side is above the oxide scale surface. The penetration of thick bumps into the Ti_2AlC substrate is caused by the inward diffusion of O^{2-}, while the outward growth of bumps is caused by the outward diffusion of Al^{3+} and Ti^{4+}. Based on the above analysis, a microstructural (Figure 10) and an atomistic (Figure 11) model can be proposed to describe the formation mechanism of oxide scale on Ti_2AlC. The characteristic structure of Ti_2AlC is layered, in which the alternate stacking of Ti_2C layers and the Al atom plane repeat (Figure 11).

At 900 ºC (Figure 10&11a), TiO_2 is formed on the surface of Ti_2AlC by inward diffusion of O^{2-} and outward diffusion of Ti^{4+} from Ti_2AlC. At 1000 ºC (Figure 10&11b), α-Al_2O_3 begins to be formed by inward diffusion of O^{2-} and outward diffusion of Al^{3+} from Ti_2AlC. Because α-Al_2O_3 is more thermodynamically stable than TiO_2, α-Al_2O_3 is more likely to be formed than TiO_2. On the other hand, compared with Ti, Al is weakly bound [32, 33] in the structure of Ti_2AlC. Therefore, it is easier for Al^{3+} to migrate from the Al atom plane in the layered structure of Ti_2AlC, than for Ti^{4+}. For these reasons, in the inner part of the oxide scale, increasing numbers of α-Al_2O_3 grains are nucleated and grow by inward diffusion of O^{2-} and outward diffusion of Al^{3+} from Ti_2AlC. As the concentration of α-Al_2O_3 rises, a continuous layer of α-Al_2O_3 is formed at the inner part of the oxide scale from 1100-1300 ºC (Figure 10&11c). In contrast, TiO_2 forms an outer discontinuous layer of oxide scale, predominating from 900-1000 ºC. Once the α-Al_2O_3 layer is formed, because the structure of α-Al_2O_3 is highly stoichiometric and highly stable, neither the inward diffusion of O^{2-} nor the outward diffusion of Al^{3+} and Ti^{4+} is suppressed. All the oxide scale becomes slow growing due to the formation of this α-Al_2O_3 layer. At 1400 ºC (Figure 10&11d), in the outer regions of the oxide scale, Al_2TiO_5 precipitates by reaction between TiO_2 and α-Al_2O_3 (Equation 1). The oxide scale outer layer becomes a mixture of TiO_2 and Al_2TiO_5. The TEC mismatch of TiO_2-Al_2TiO_5 is so large (rutile: $\alpha_a = 9.2 \times 10^{-6}\ K^{-1}$, $\alpha_c = 7.1 \times 10^{-6}\ K^{-1}$; Al_2TiO_5: $\alpha_a = 10.9 \times 10^{-6}\ K^{-1}$, $\alpha_b = 20.5 \times 10^{-6}\ K^{-1}$, $\alpha_c = -2.7 \times 10^{-6}\ K^{-1}$ [21]) and, along with the TEC anisotropy in Al_2TiO_5 grains and the volume changes associated with the reactions during Ti_2AlC oxidation, that it causes cracks which propagate into α-Al_2O_3 grains (small arrows in Figure 6a). The inner α-Al_2O_3 layer thus becomes cracked, providing channels for rapid ingress of oxygen to the body (Figure 10&11d). Oxygen passes through these cracks, and then reacts with Al^{3+} and Ti^{4+} from Ti_2AlC to

form α-Al_2O_3 and TiO_2, leading to heavy oxidation at 1400 ºC.

The oxidation resistance of high-temperature ceramics and alloys is dependent on the formation of a protective surface oxide. In an ideal case, the oxide layer should be highly stable, slow growing, free from pores or cracks, adherent and coherent [10]. α-Al_2O_3 is an oxide which comes close to satisfying these requirements. Between 1100-1300 ºC, a continuous, stable and crack-free α-Al_2O_3 layer is formed in the oxide scale (Figure 10&11c). Such an α-Al_2O_3 layer is protective preventing Ti_2AlC from further extensive oxidation. In addition, the coefficients of thermal expansion of Ti_2AlC (α_a= (7.1±0.3) ×10^{-6} K^{-1}, α_c= (10±0.5) ×10^{-6} K^{-1}) [23] and α-Al_2O_3 (α_a= 7.9 ×10^{-6} K^{-1}, α_c =8.8 ×10^{-6} K^{-1}) are small in magnitude, so generating low thermal stresses at the α-Al_2O_3/Ti_2AlC interface during oxidation. However, the large TEC mismatch of TiO_2-Al_2TiO_5, the TEC anisotropy in Al_2TiO_5 grains, and along with the large volume changes associate with the reactions during Ti_2AlC oxidation reactions, causes cracks which propagate into the α-Al_2O_3 layer (Figure 6a), making it non-protective for Ti_2AlC at 1400 ºC. Therefore, the oxidation resistance of Ti_2AlC is limited up to 1400 ºC. The cracks increase the ingress of oxygen into the body. Therefore, when the temperatures are higher than 1400 ºC, Ti_2AlC undergoes heavy oxidation because O_2 can pass through these cracks in the oxide scale to react with Ti_2AlC.

4. Conclusions

(1) Microstructural development during high-temperature oxidation of Ti_2AlC has been investigated. Below 1300 ºC, a discontinuous outer TiO_2 layer and a dense and continuous inner α-Al_2O_3 layer were gradually formed. After heating at 1400 ºC, a mixed outer layer of TiO_2 and Al_2TiO_5 and a cracked α-Al_2O_3 inner layer were formed.

(2) After heating at 1200 ºC, two types of planar defect have been identified in surface TiO_2 grains: twins with (2 0 0) twin plane and stacking faults bounded by partial dislocations. The formation of planar defects is believed to be related to thermal stresses generated in TiO_2 grains, arising from thermal expansion mismatch of phases in the oxide scale. The planar defects were annealed out by 1400 ºC.

(3) After heating to 1400ºC, the large TEC mismatch of TiO_2-Al_2TiO_5, the TEC anisotropy in

Al_2TiO_5 grains, along with the large volume changes associate with the reactions resulted in cracks in TiO_2 grains which propagate into the α-Al_2O_3 layer.

(4) An atomistic model is proposed to describe the formation mechanism of oxide scale on Ti_2AlC, in which the growth of oxide scale is caused by inward diffusion of O^{2-} and outward diffusion of Al^{3+} and Ti^{4+}. The weakly bound Al leaves the Al atom plane in the layered structure of Ti_2AlC, and diffuses outward to form a protective inner α-Al_2O_3 layer between 1100 and 1300 ºC. However, due to the crack propagation the α-Al_2O_3 layer becomes cracked at 1400 ºC, providing channels for rapid ingress of oxygen to the body, leading to heavy oxidation.

Acknowledgment

The authors gratefully acknowledge the Lee Family Scholarship for financial support. B. Cui would like to express gratitude for Dr Mahmoud Ardakani and Richard Chater for their help in TEM and FIB, and thank Prof. Yanchun Zhou (Shenyang National Laboratory for Materials Science, CAS) for providing Ti_2AlC samples. The reviewers and Dr. Mary Ryan are thanked for valuable comments and discussions.

References

[1] Barsoum MW. Prog Solid State Chem 2000; 28: 201.

[2] Barsoum MW, El-Raghy T. Am Scientist 2001; 89: 334.

[3] Wang J, Zhou Y. Annu Rev Mater Res 2009; 39: 415.

[4] Wang X, Zhou Y. J Mater Sci Technol 2010; 26: 385.

[5] Sundberg M, Malmqvist G, Magnusson A, El-Raghy T. Ceram Int 2004; 30: 1899.

[6] Barnes LA, Rago NLD, Leibowitz L. J Nuclear Mater 2008; 373: 424.

[7] Barsoum MW, Tzenov N, Procopio A, El-Raghy T, Ali M. J Electrochem Soc 2001; 148: 551.

[8] Wang X, Zhou Y. Oxid Met 2003; 59: 303.

[9] Wang X, Zhou Y. J Mater Res 2002; 17: 2974.

[10] Prescott R, Graham MJ. Oxid Met 1992; 38: 233.

[11] Wang X, Zhou Y. Z Metalkd 2002; 93: 66.

[12] Somani V, Kalita SJ. J Am Ceram Soc 2007; 90: 2372.

[13] Wang X, Zhou Y. Corros Sci 2002; 45: 891.

[14] Russ JC, Dehoff RT. Practical stereology. New York: Kluwer Academic/ Plenum Publishers, 2000.

[15] Lekstrom M, McLachlan MA, Husain S, McComb DW, Shollock BA. J Phys: Conf Ser 2008; 126: 12028.

[16] Langford RM. Microsc Res Tech 2006; 69: 538.

[17] Woignier T, Lespade P, Phalippou J, Rogier R. J Non-cryst Solids 1988; 100: 325.

[18] McCoy MA, Dregia SA, Lee WE. J Mater Res 1994; 9: 2040.

[19] Hirsch PB, Howie A, Nicholson RB, Pashley DW, Whelan ML. Electron microscopy of thin crystals. London: Butterworths; 1967.

[20] Lee WE, Reaney IM, McCoy MA. Br Ceram Proc 1996; 55: 199.

[21] Taylor D. Br Ceram Trans J 1987; 86: 1.

[22] Morosin B, Lynch RW. Acta Crystallorgr B 1972; 25: 1040.

[23] Barsoum MW, Ali M, El-Raghy T. Met Mat Trans A 2000; 31: 1857.

[24] Hasselman DPH. J Am Ceram Soc 1969; 52: 600.

[25] Wachtman JB, Cannon WR, Matthewson MJ. Mechanical properties of ceramics. New York:

John Wiley & Sons; 2009.

[26] Barsoum MW. Fundamentals of ceramics. New York: McGraw Hill; 1997.

[27] Ohya Y, Nakagawa Z, Hamano K. J Am Ceram Soc 1987; 70: 184.

[28] Lee WE, Rainforth WM. Ceramic microstructures: Property control by processing. London: Chapman & Hall; 1994.

[29] Barsoum MW. J Electrochem Soc 2001; 148: 544.

[30] Barsoum MW, Tzenov N, Procopio A, El-Raghy T, Ali M. J Electrochem Soc 2001; 148: 551.

[31] Wang X, Zhou Y. J Mater Sci Technol 2010; 26: 385.

[32] Hug G. Phys Rev B 2006; 74: 184113.

[33] Liao T, Wang J, Zhou Y. J Mater Res 2009; 24: 556.

Table 1. Phase composition of the samples oxidized at temperatures of 900-1400 ºC.

Oxidation temperature (ºC)	Normalized intensity of the highest diffraction peaks of each phase (%)			
	Ti_2AlC (1 0 3)	TiO_2 (rutile) (1 1 0)	α-Al_2O_3 (1 1 3)	Al_2TiO_5 (1 1 0)
900	94.9 ± 0.3	5.1 ± 0.3	0	0
1000	86.4 ± 0.4	9.0 ± 0.2	4.6 ± 0.2	0
1200	82.2 ± 0.3	7.0 ± 0.1	10.8 ± 0.2	0
1400	43.7 ± 0.2	5.9 ± 0.1	38.7 ± 0.2	11.7 ± 0.1

Figure Captions

Figure 1. XRD after oxidation of Ti_2AlC at temperatures from 900 to 1400 ºC in air for 1 h. TiO_2 (rutile) and α-Al_2O_3 start to be detected in the oxide scale after oxidation at 900-1000 ºC, Al_2TiO_5 is initially present at 1400 ºC.

Figure 2. TG showing a significant mass increase near 940 ºC (at a heating rate of 20 ºC min^{-1}) or 920 ºC (at 10 ºC min^{-1}) which is associated with TiO_2 (rutile) formation. The DTG peak at 1009.8 ºC (at 20 ºC min^{-1}) or 999.2 ºC (at 10 ºC min^{-1}) is likely associated with formation of α-Al_2O_3.

Figure 3. Typical SEI surface morphology of Ti_2AlC oxidized at (a) 900 ºC, (b) 1000 ºC, (c) 1200 ºC, (d) 1300 ºC and (e) 1400 ºC. Arrows in d) and e) indicate cracks.

Figure 4. (a) Cross-section SEM image of a Ti_2AlC sample oxidized in air at 1000 ºC. (b) EDS line-scanning profiles along the black arrow in a). (c) EDS line-scanning profiles along the grey arrow in a).

Figure 5. (a) Cross-section SEM image of a Ti_2AlC sample oxidized in air at 1200 ºC. (b) EDS line-scanning profiles along the black arrow in a).

Figure 6. (a) Cross-section SEM image of a Ti_2AlC sample oxidized in air at 1400 ºC indicating cracks (small arrows) in α-Al_2O_3 layer. (b) EDS line-scanning profiles along the vertical black arrow in a).

Figure 7. (a) BF image of the TiO_2 microtwins for sample oxidized at 1200 ºC. (b) Corresponding SAED patterns along the [0 1 1] rutile direction. (c) Indexed schematic.

Figure 8. BF (a) and DF (b) images of the stacking faults in TiO_2 grains, recorded with **g**=1 0 -1 along the rutile [1 1 1] zone axis. Arrows in b) indicate partial dislocations. (c) Corresponding SAED patterns along the rutile [1 1 1] zone axis. (d) HRTEM image of stacking faults recorded along the [0 1 1] zone axis.

Figure 9. Typical SEI surface morphology of Ti_2AlC samples after (a) cyclic oxidation and (b) isothermal oxidation at 1400 ºC. Arrows in a) and b) indicate cracks.

Figure 10. Schematic illustration summarizing the microstructural evolution during Ti_2AlC oxidation.

Figure 1. Schematic illustration of an atomistic model describing the formation mechanism of

oxide scale on Ti_2AlC.

(All color figures are intended to be reproduced in color on the Web and in black-and-white in print.)

Figure 1

Click here to download high resolution image

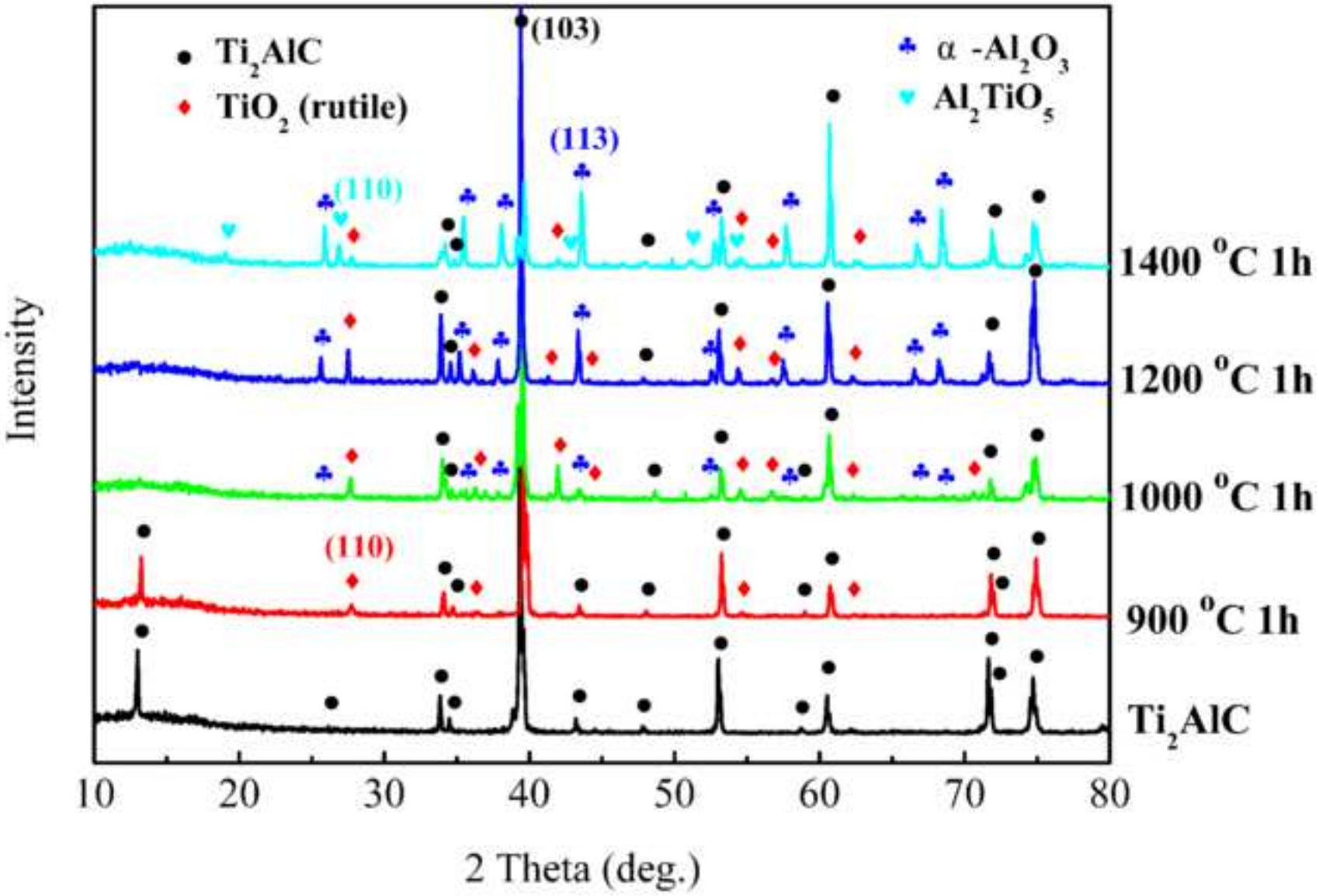

Figure 2

Click here to download high resolution image

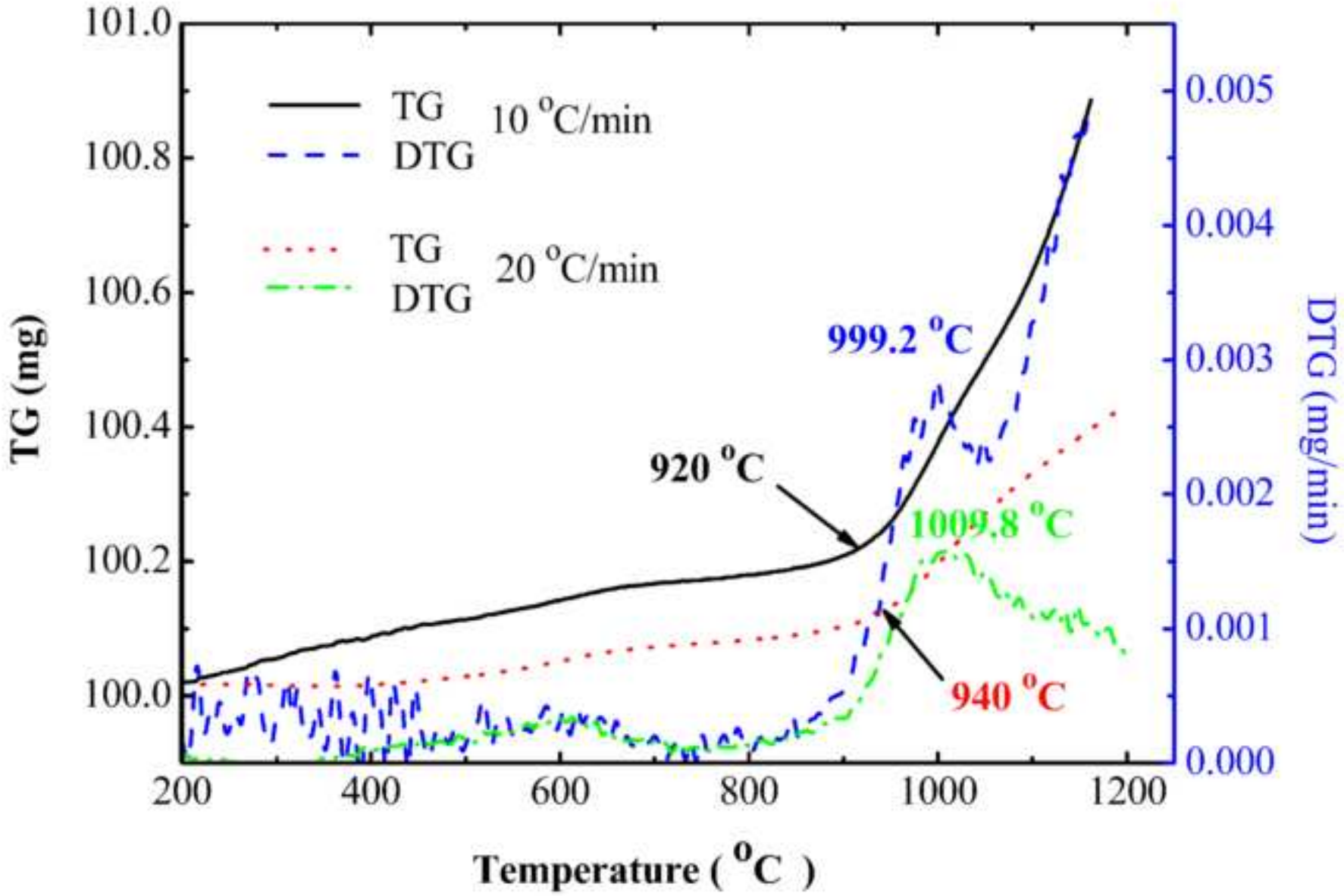

Figure 3a

Click here to download high resolution image

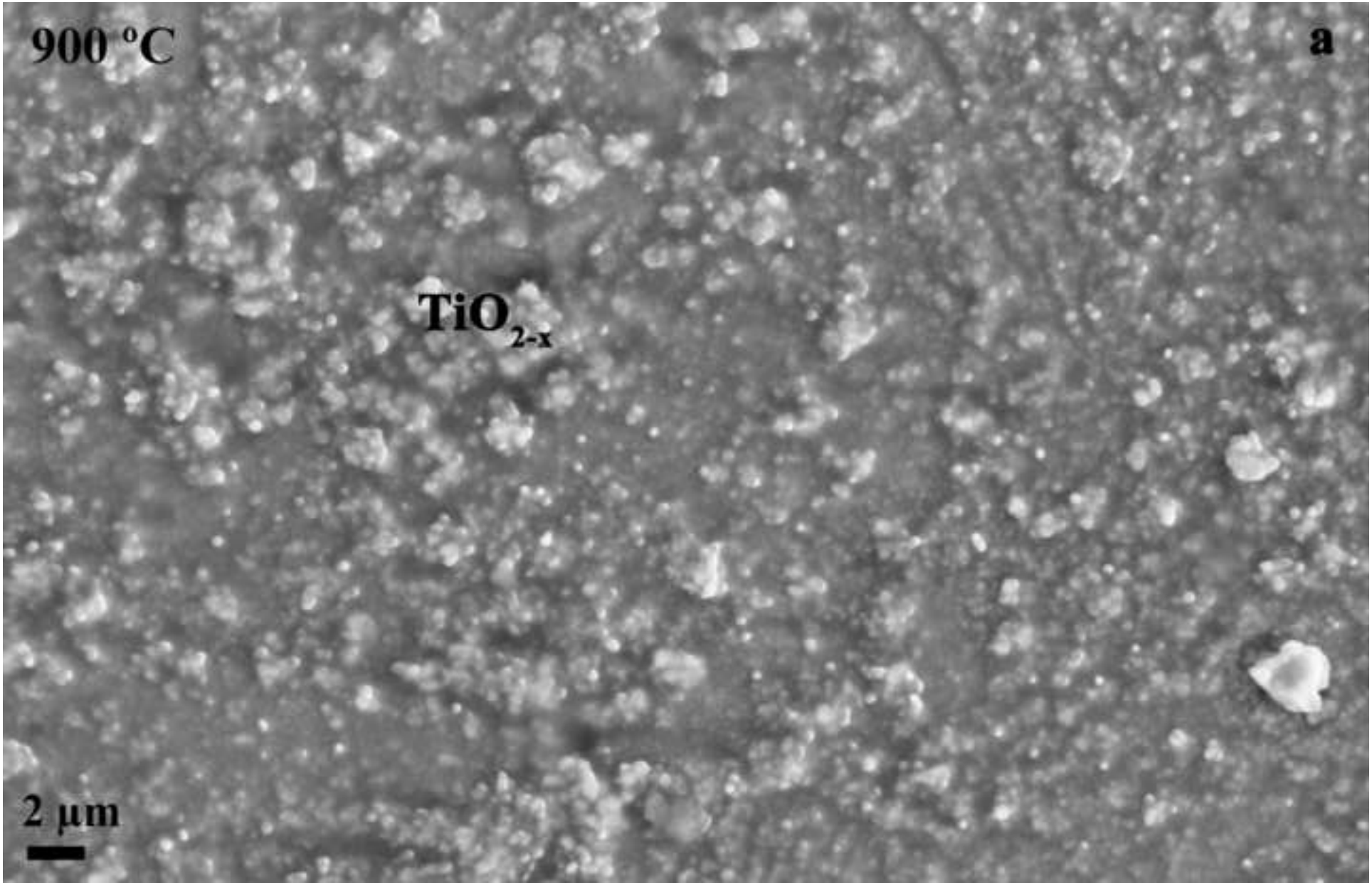

Figure 3b

Click here to download high resolution image

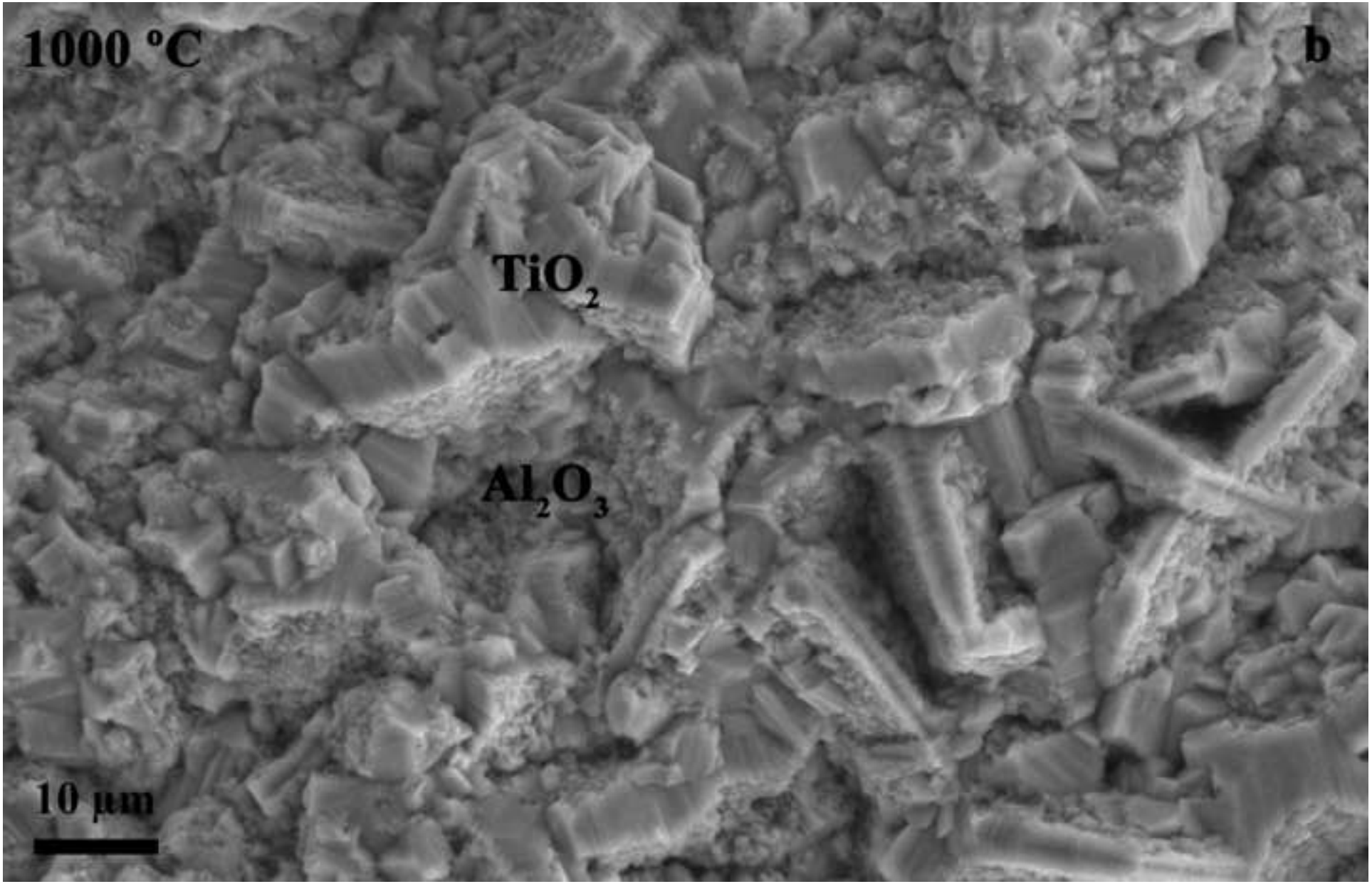

Figure 3c

Click here to download high resolution image

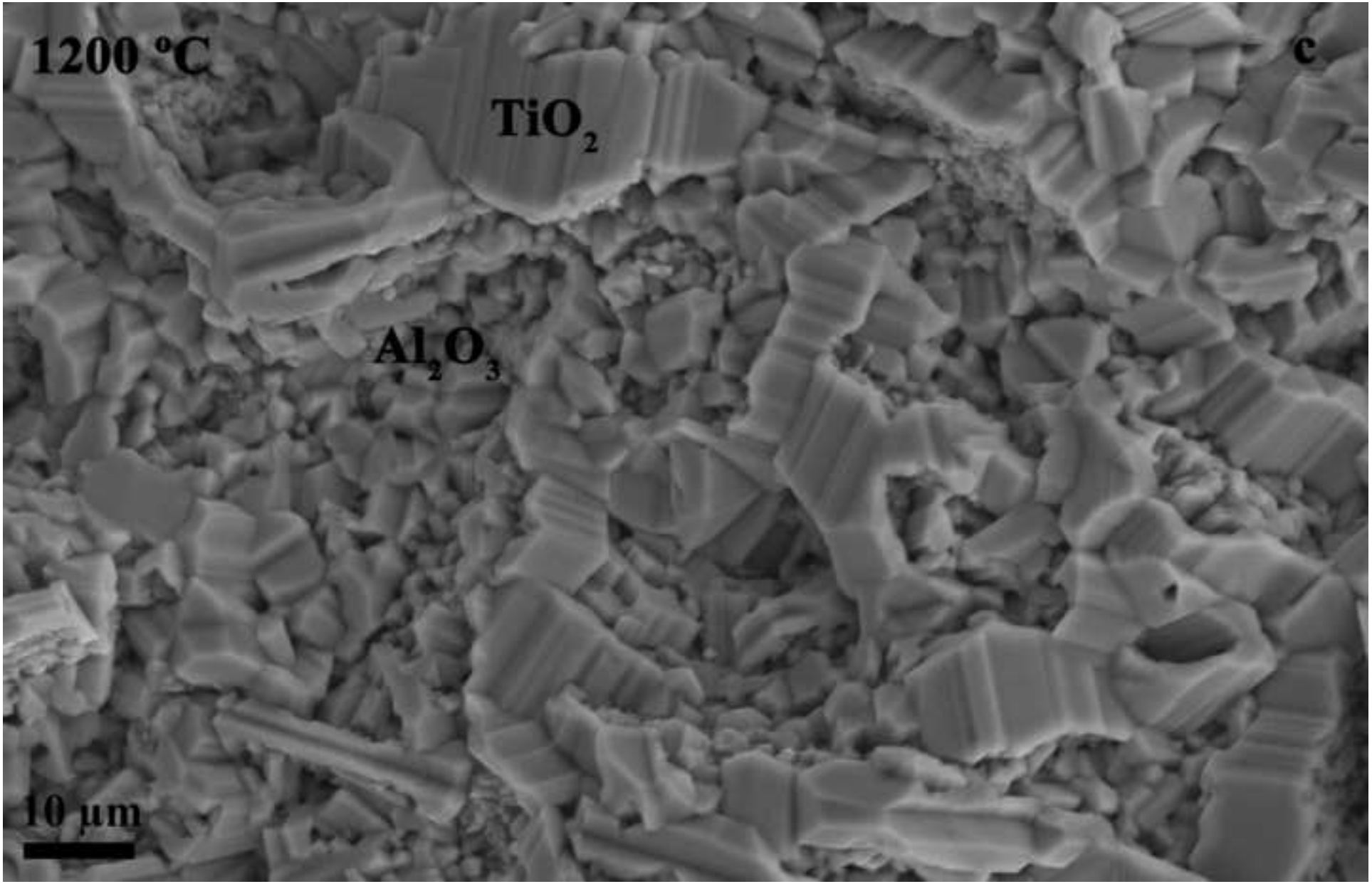

Figure 3d
Click here to download high resolution image

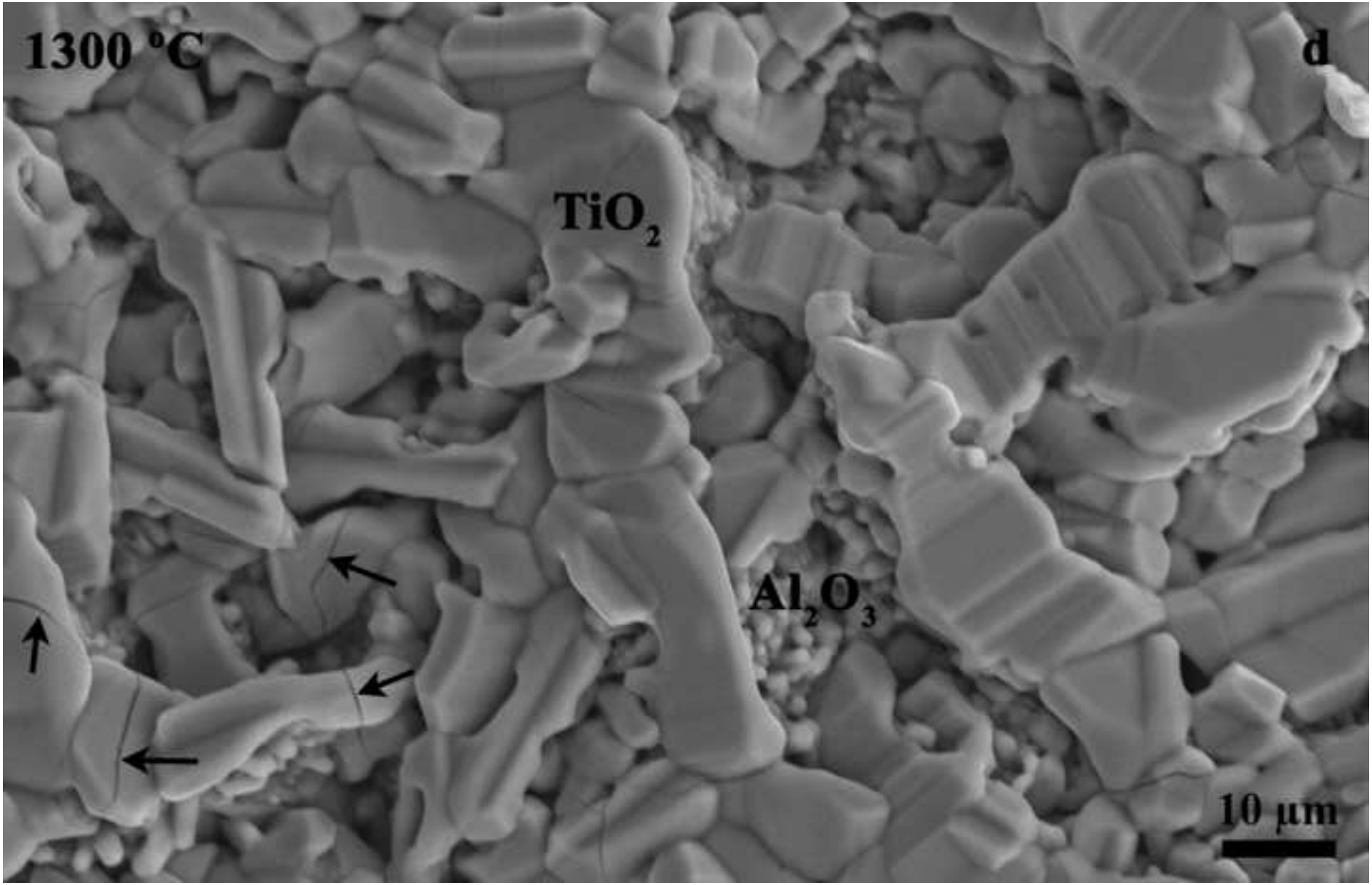

Figure 3e

Click here to download high resolution image

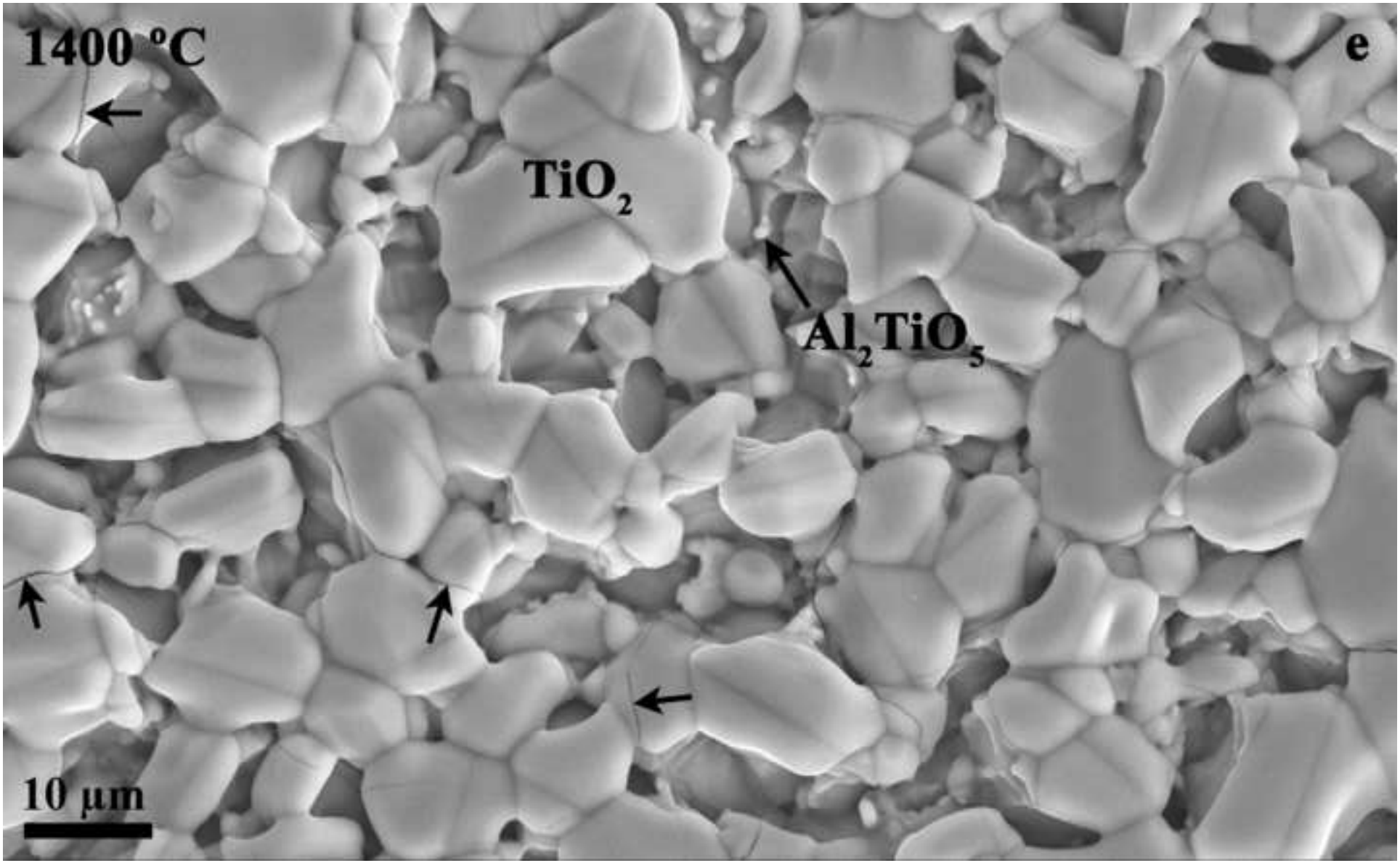

Figure 4a
Click here to download high resolution image

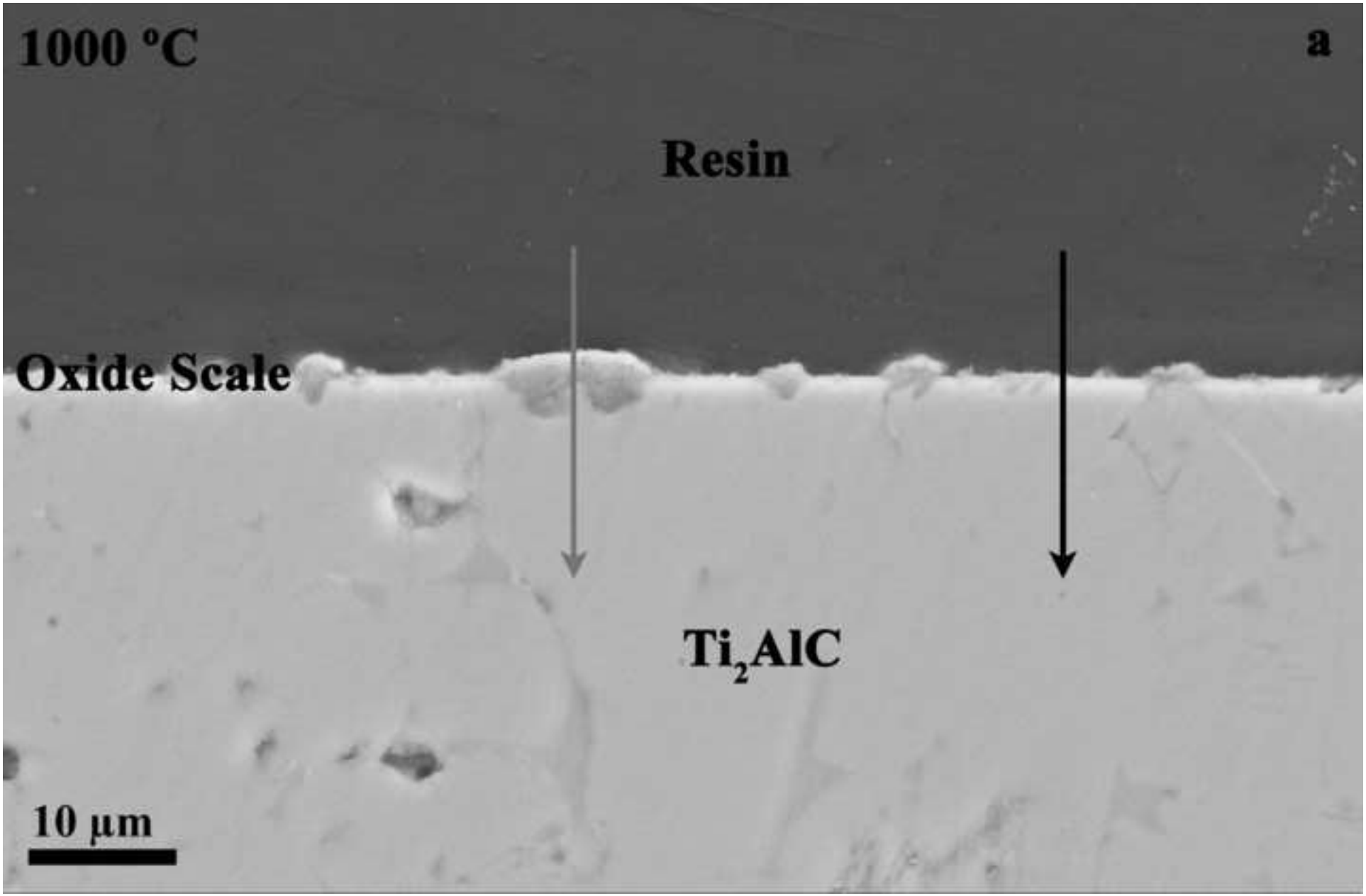

Figure 4b

Click here to download high resolution image

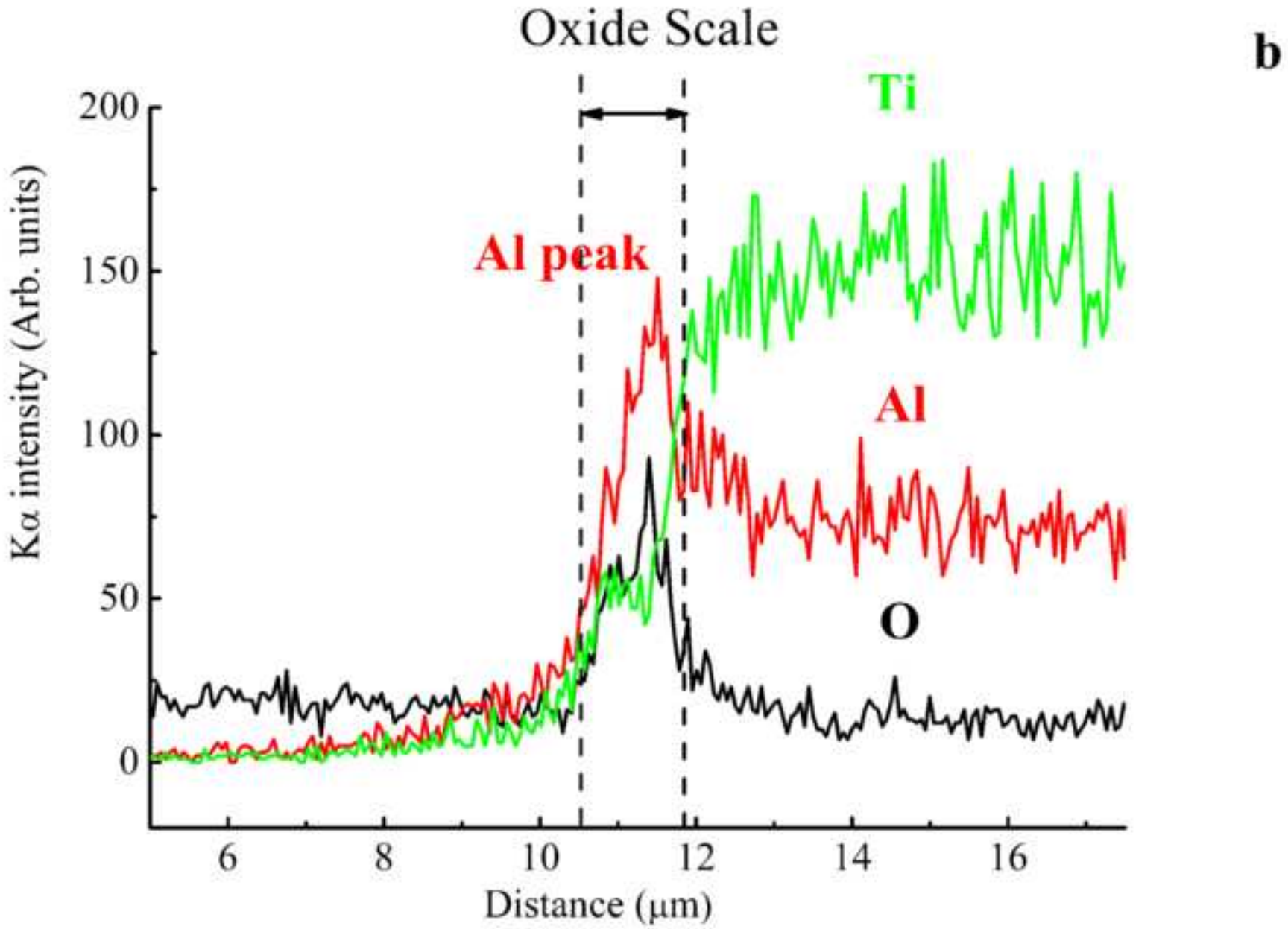

Figure 4c
Click here to download high resolution image

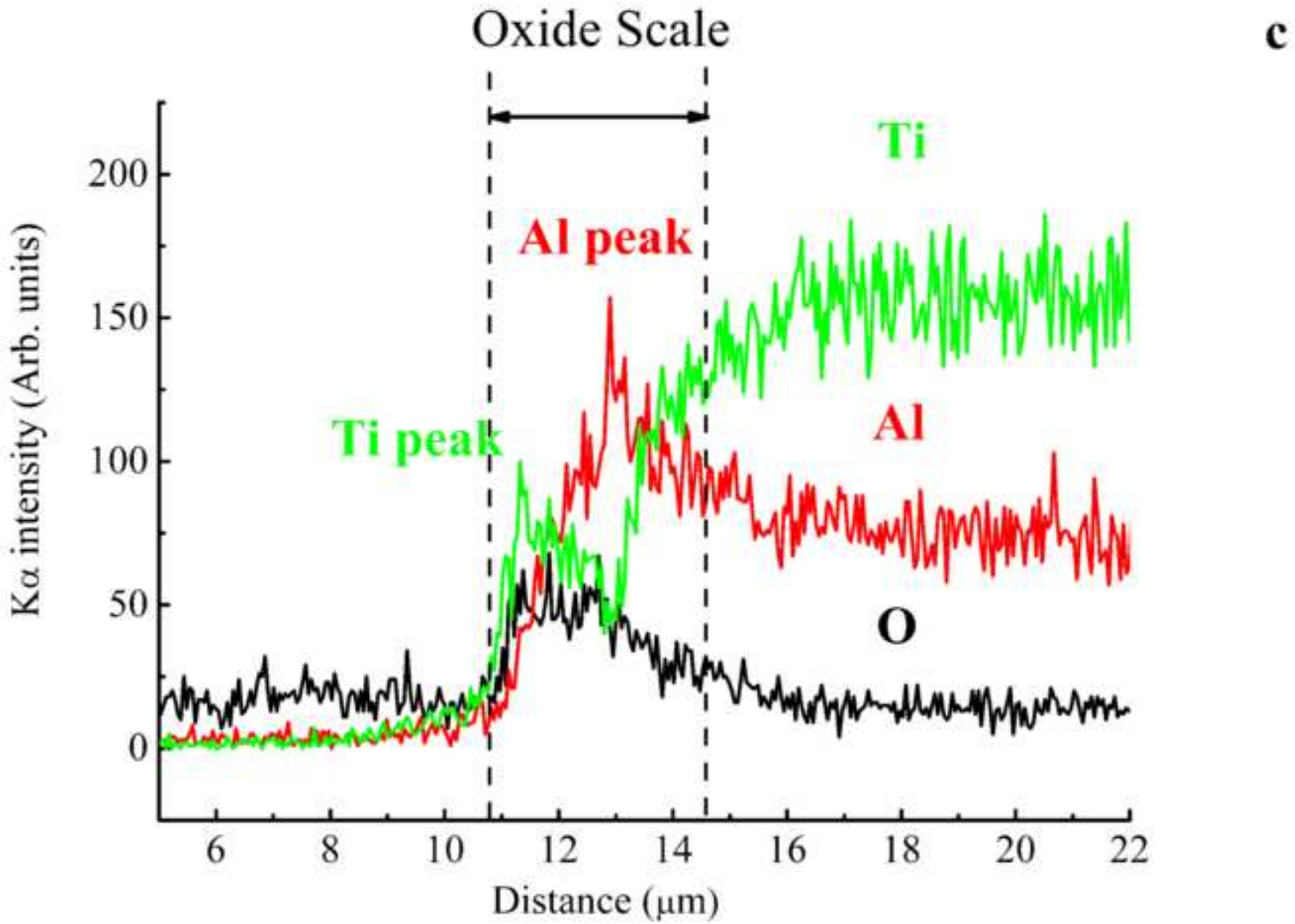

Figure 5a
Click here to download high resolution image

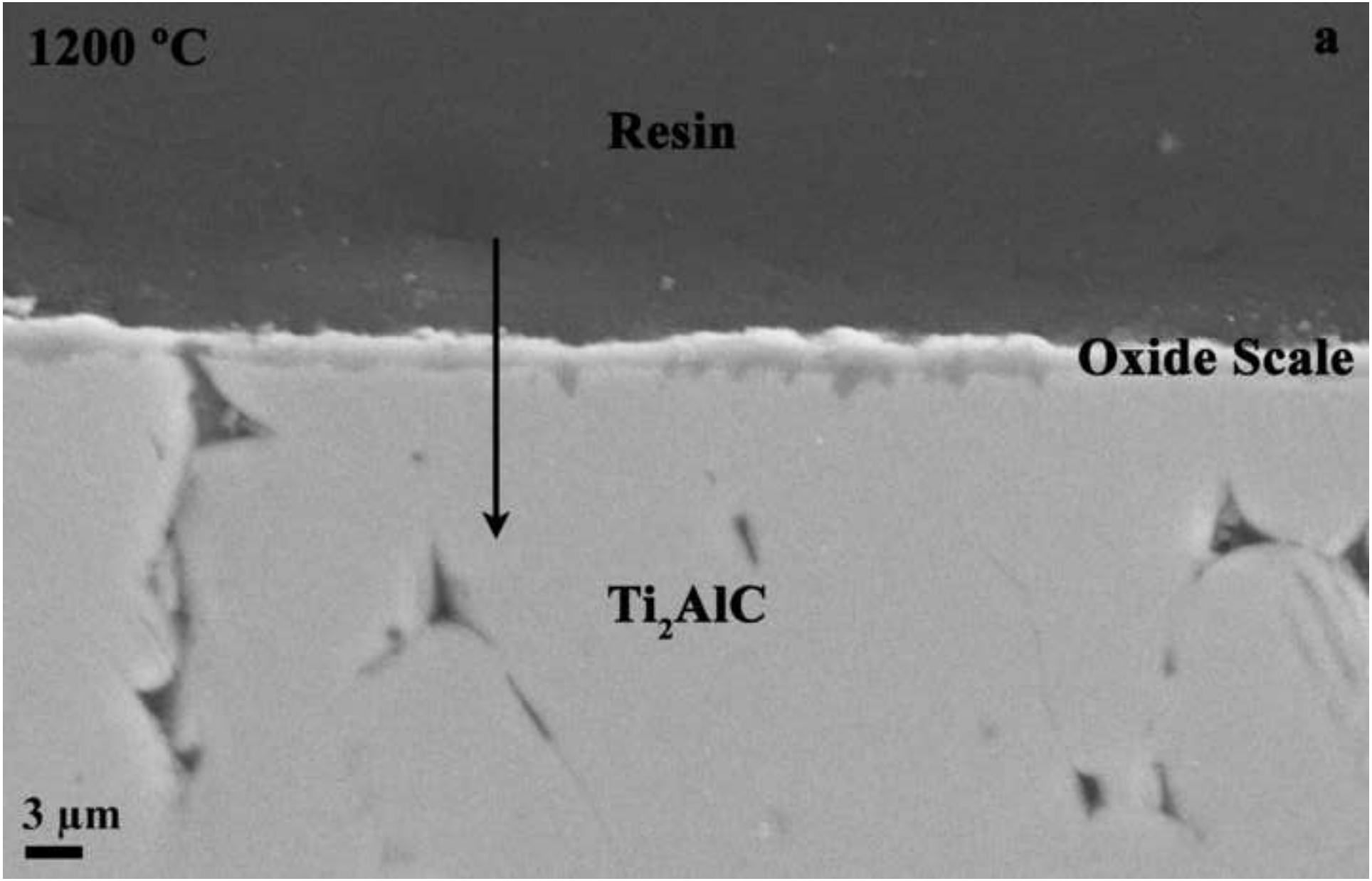

Figure 5b
Click here to download high resolution image

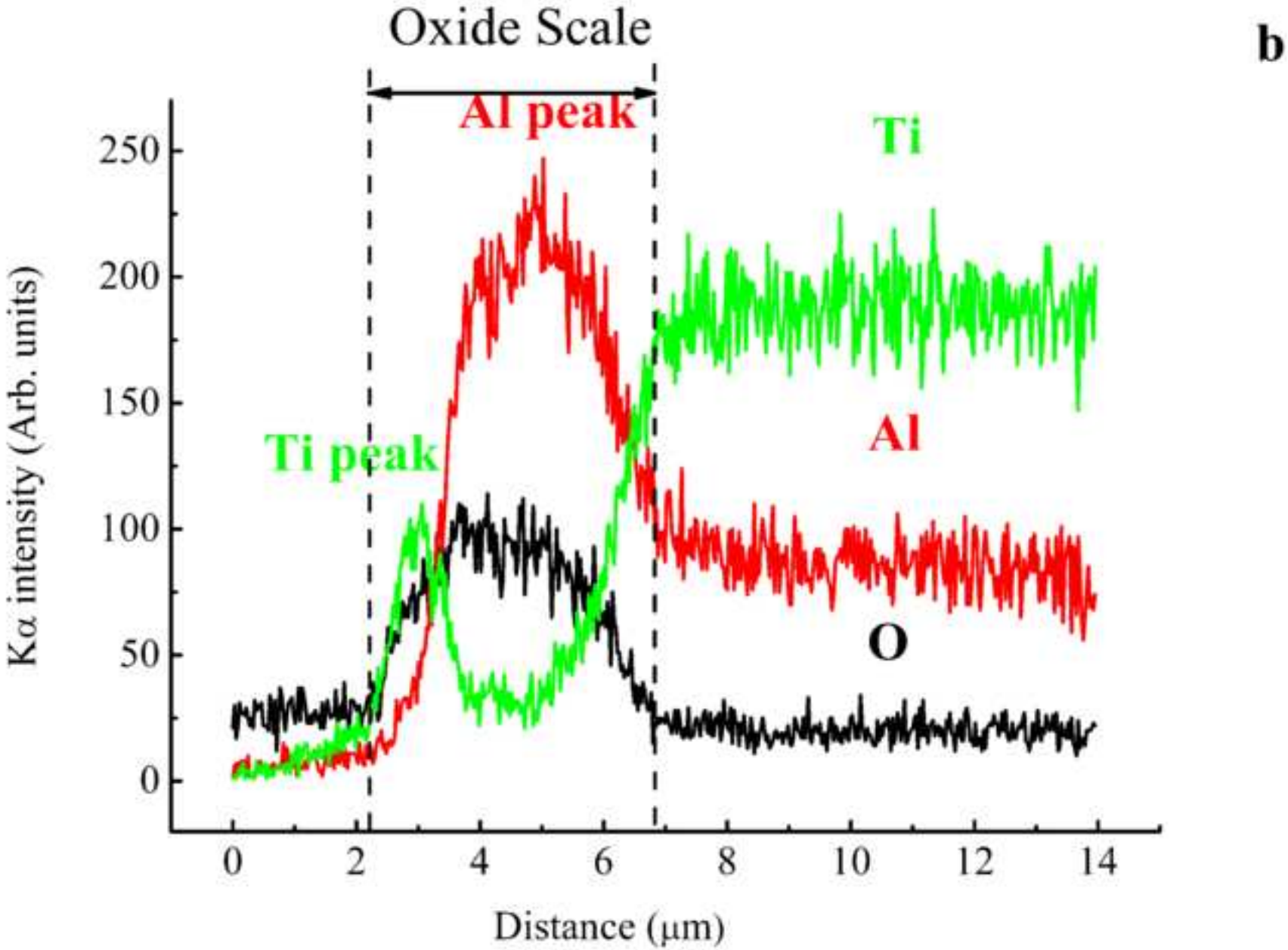

Figure 6a
Click here to download high resolution image

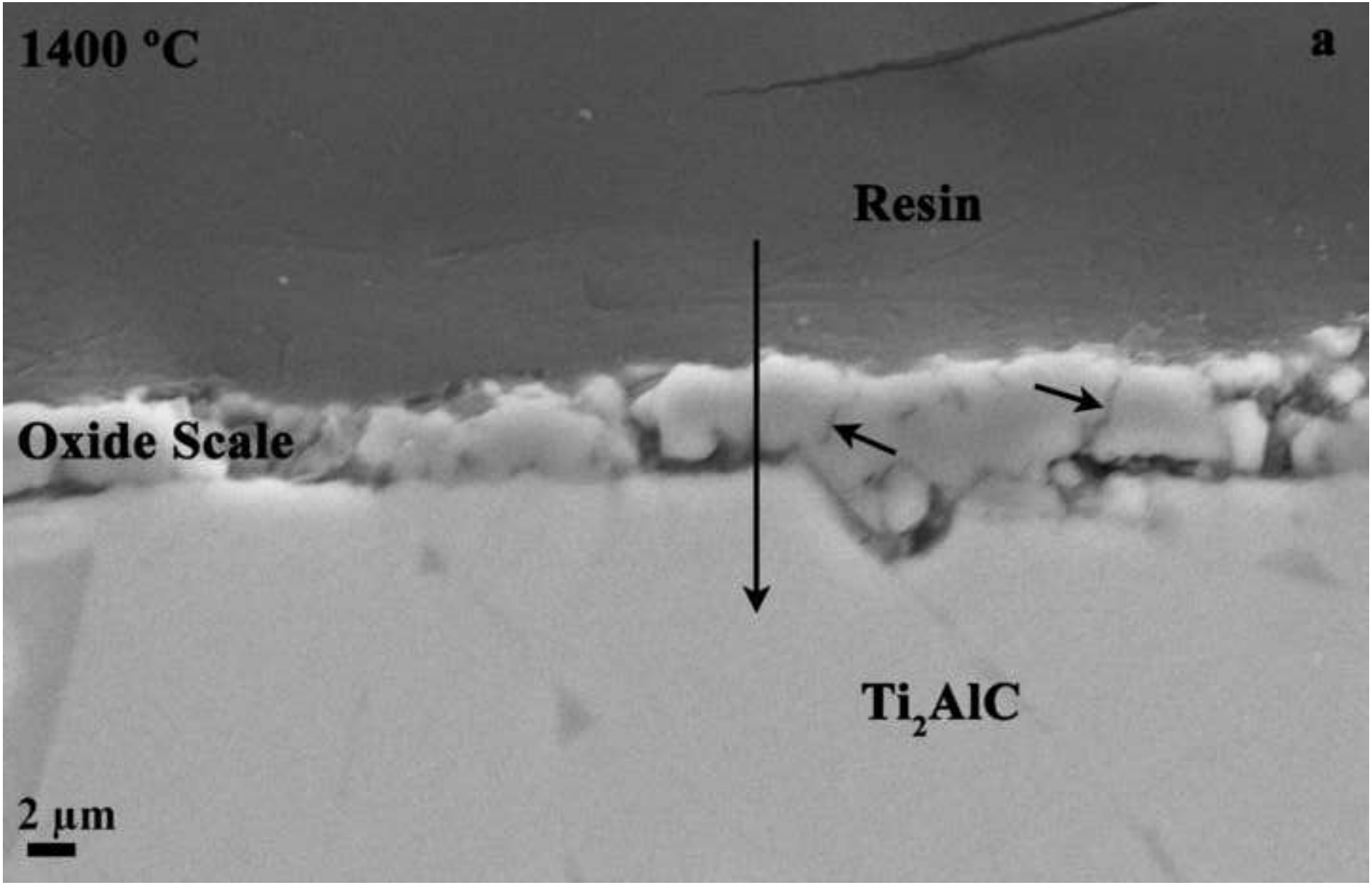

Figure 6b

Click here to download high resolution image

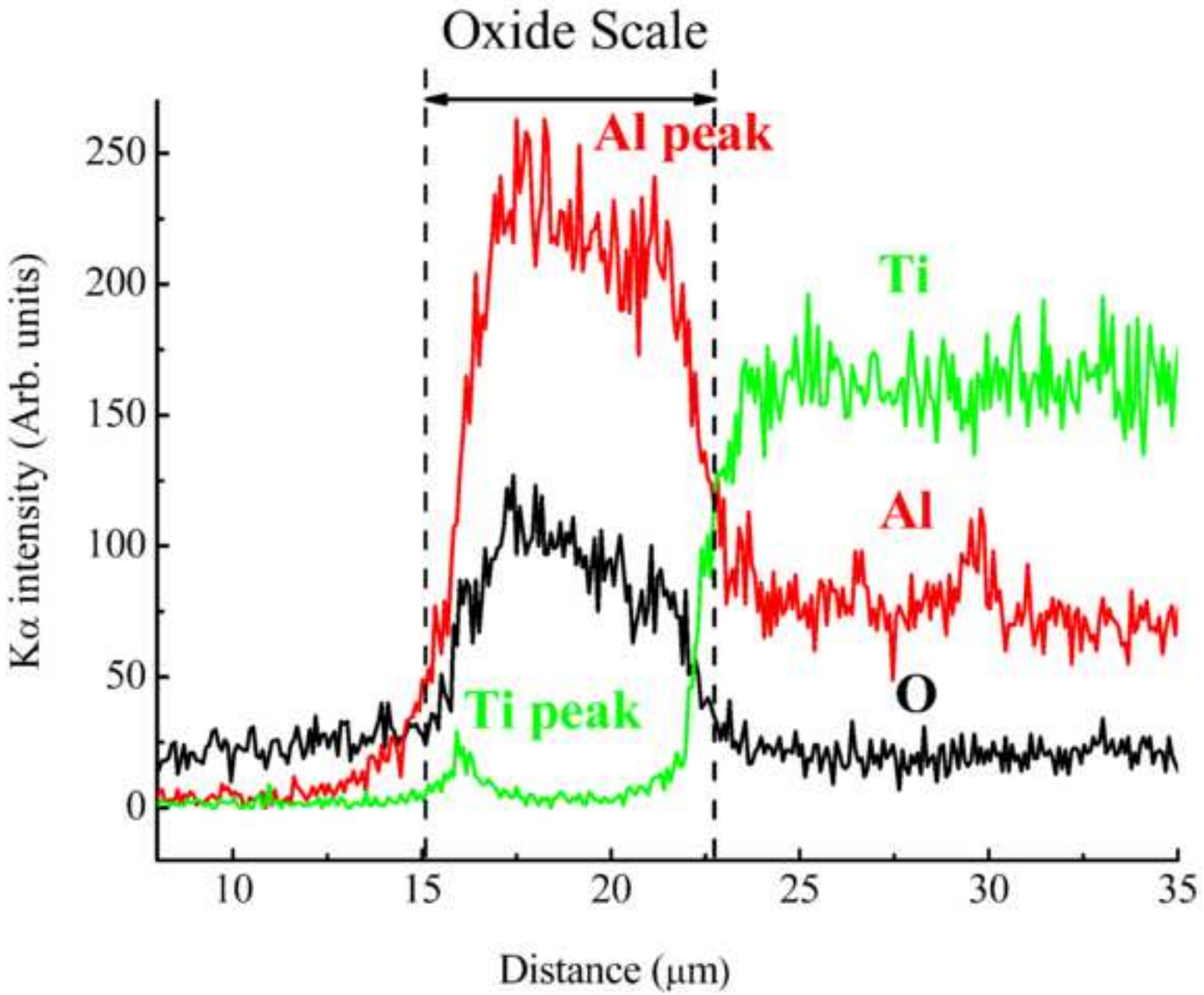

Figure 7a
Click here to download high resolution image

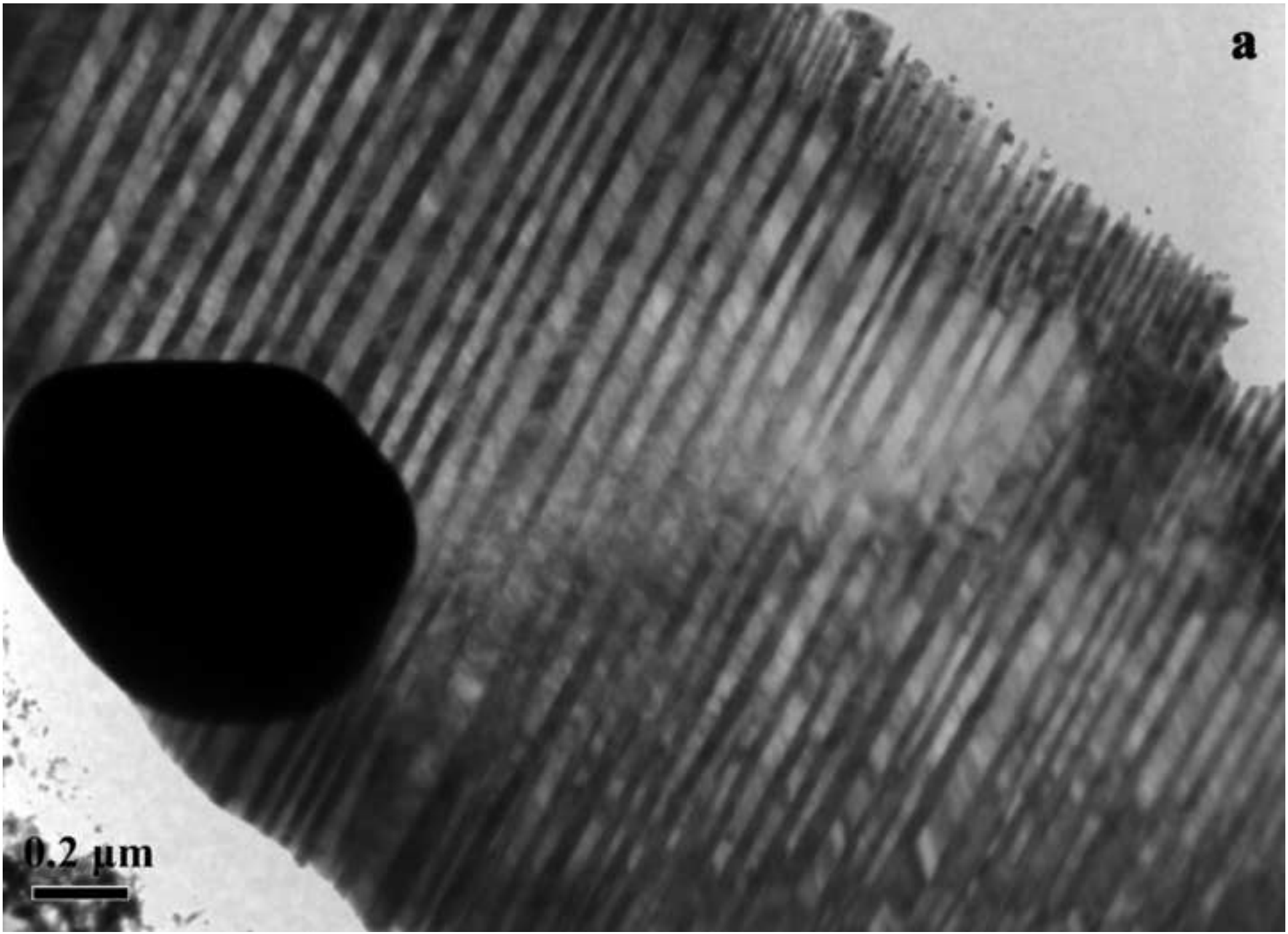

Figure 7b

Click here to download high resolution image

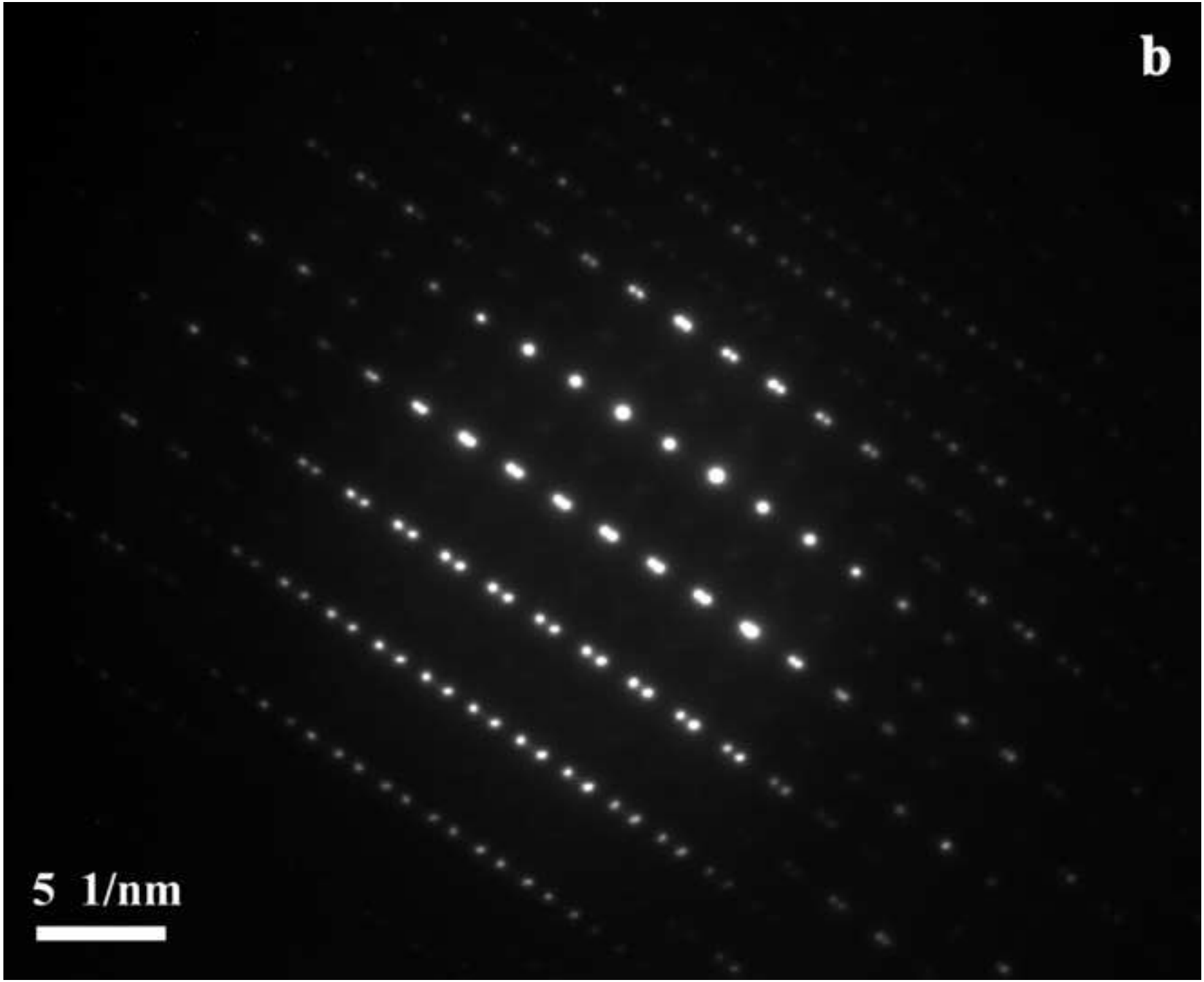

Figure 7c

Click here to download high resolution image

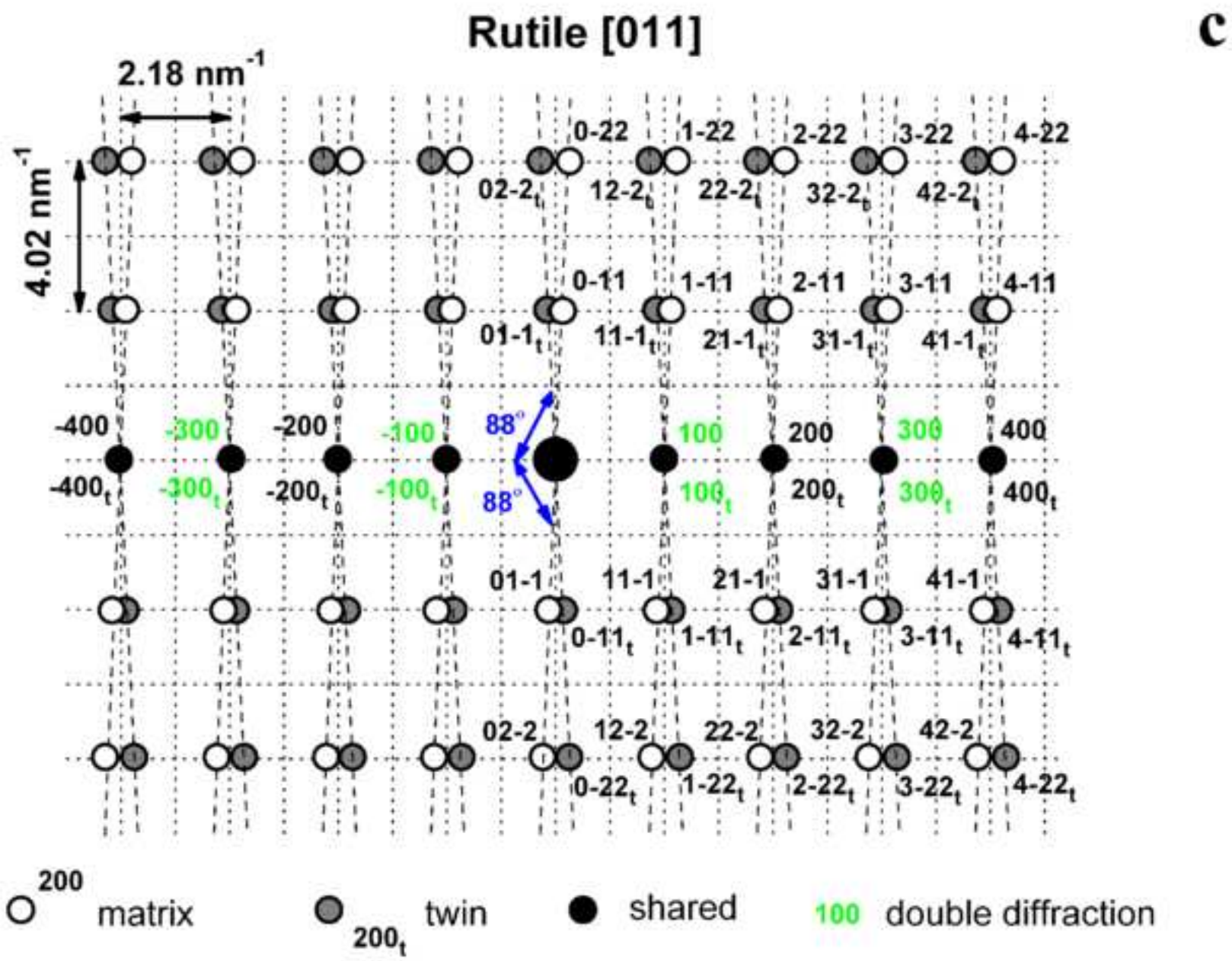

Figure 8a

Click here to download high resolution image

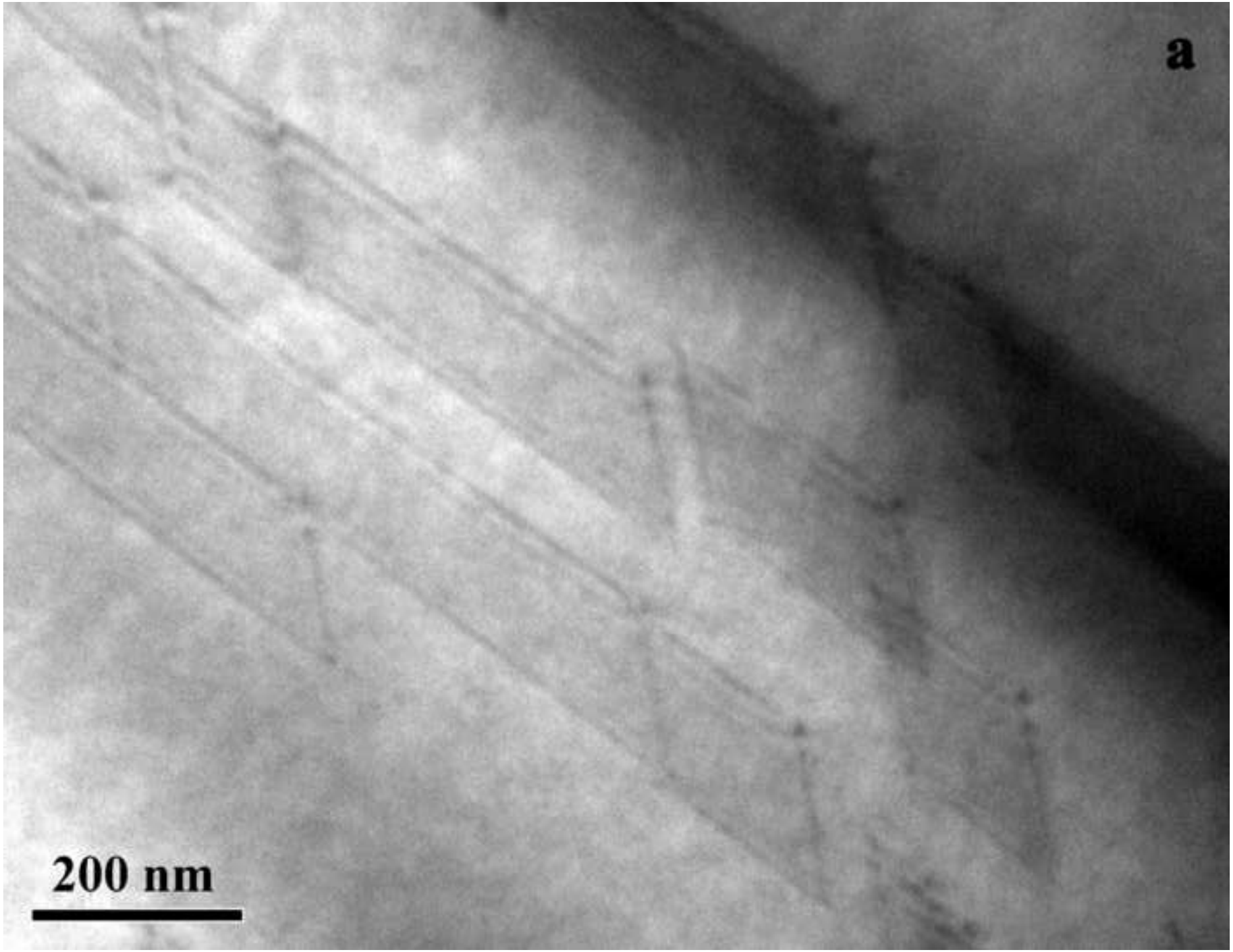

Figure 8b

Click here to download high resolution image

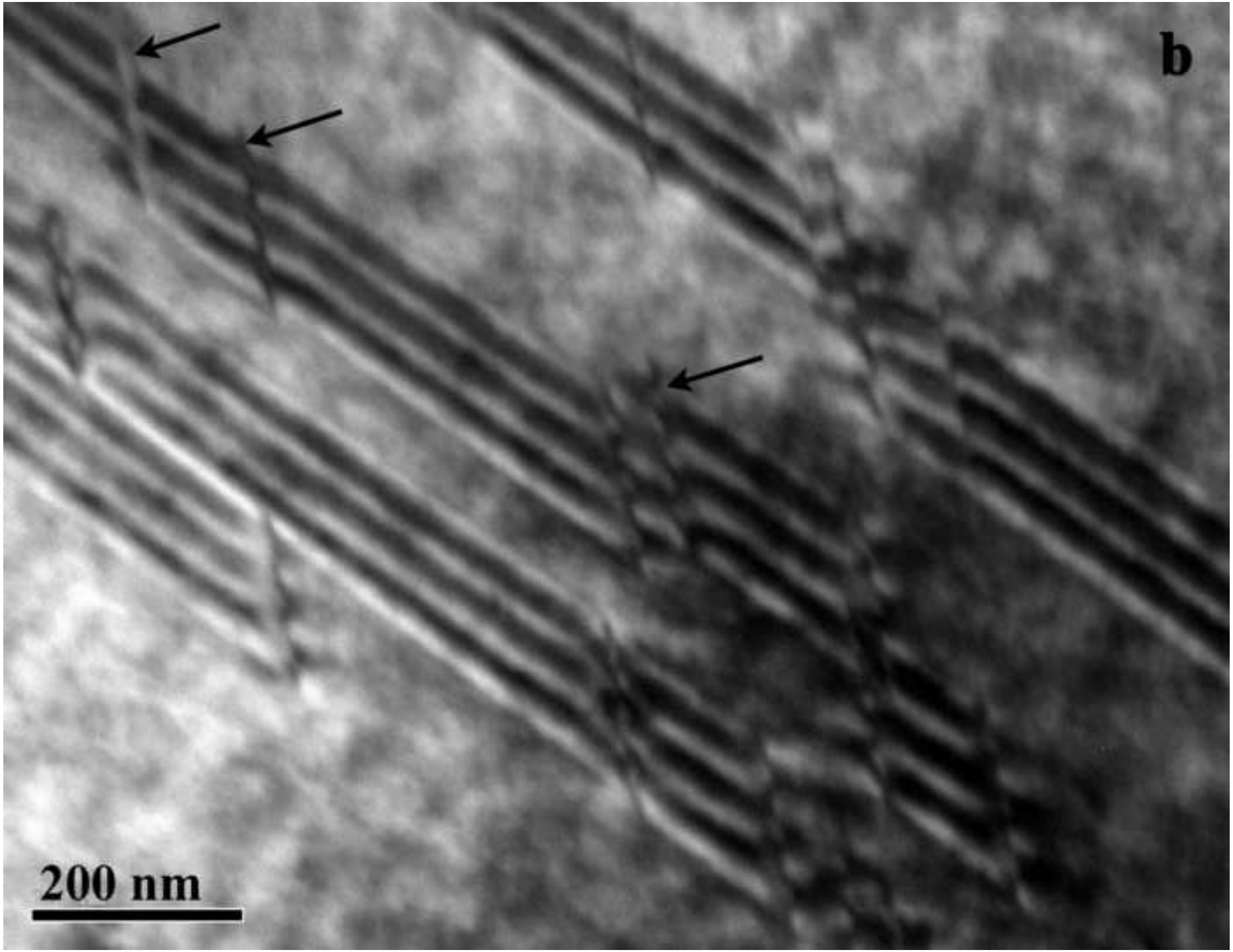

Figure 8c

Click here to download high resolution image

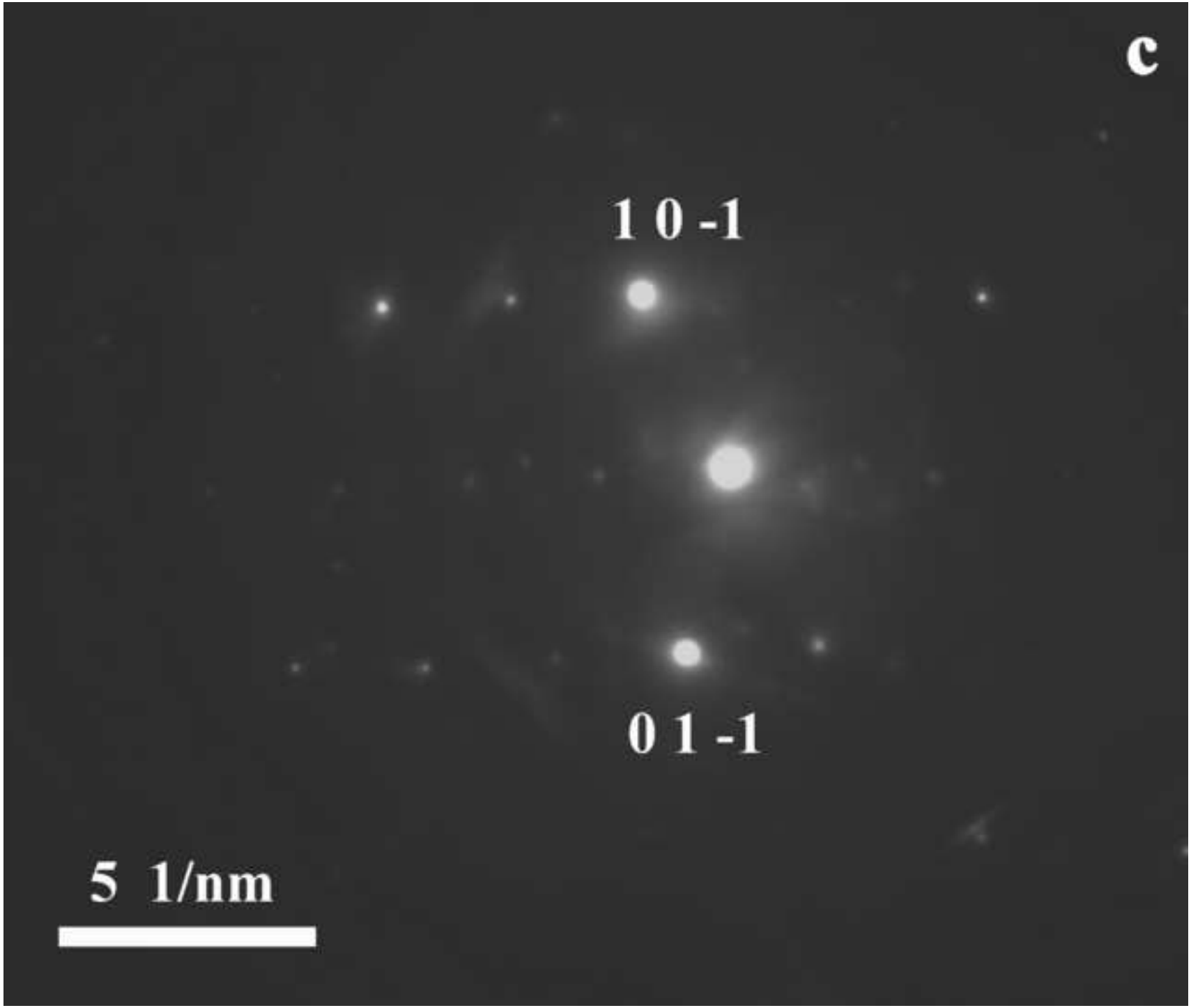

Figure 8d

Click here to download high resolution image

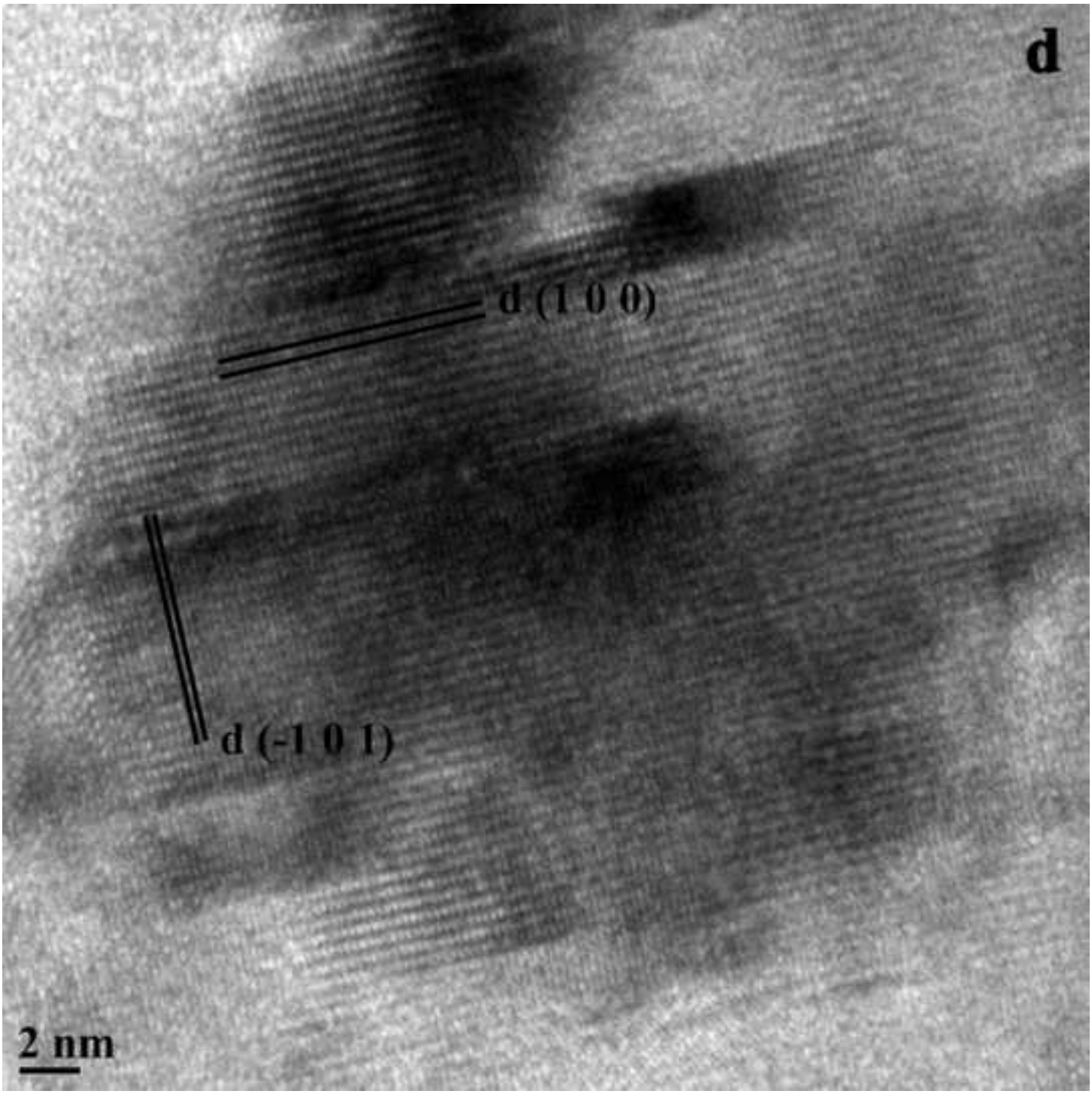

Figure 9a

Click here to download high resolution image

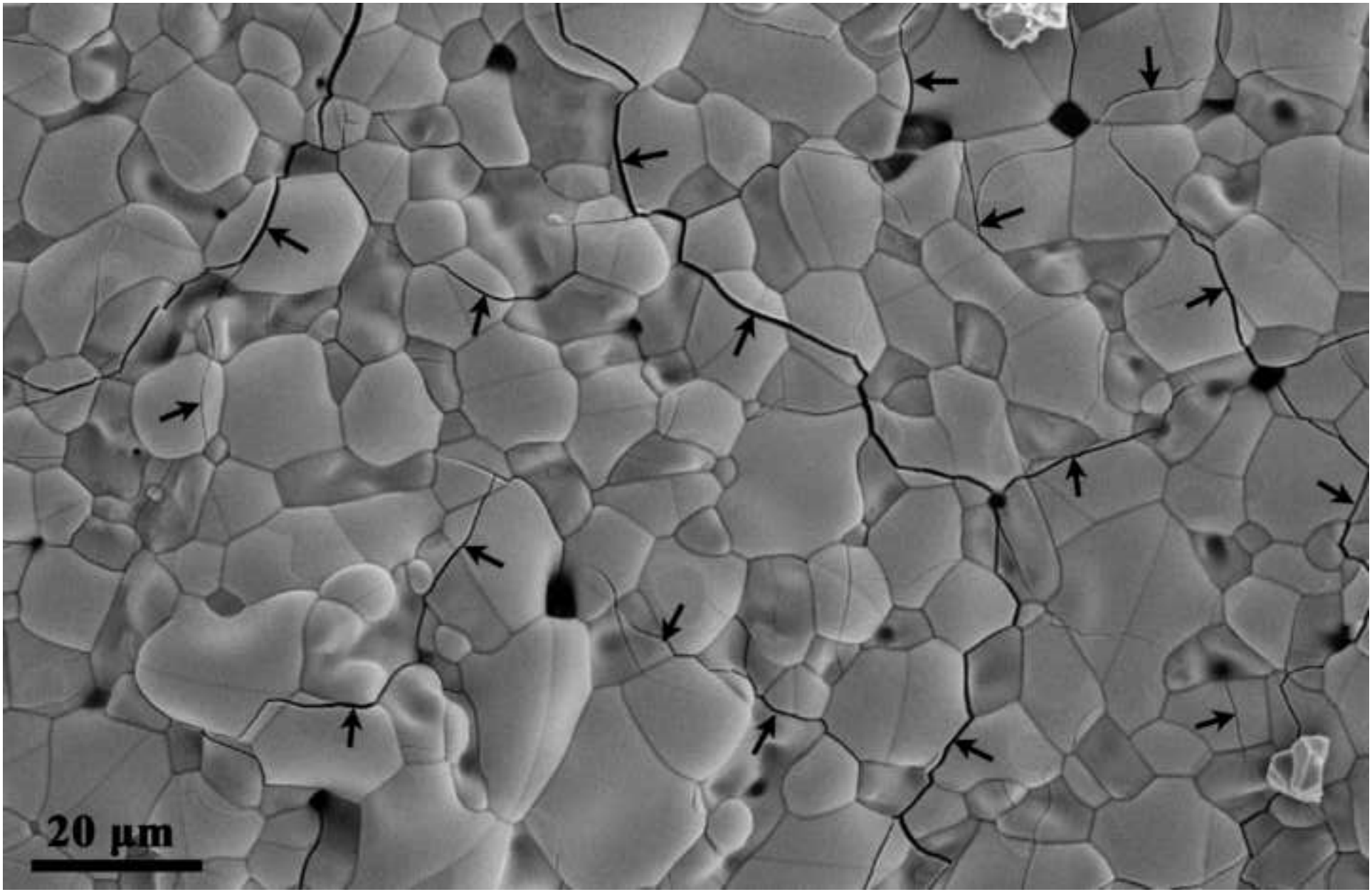

Figure 9b

Click here to download high resolution image

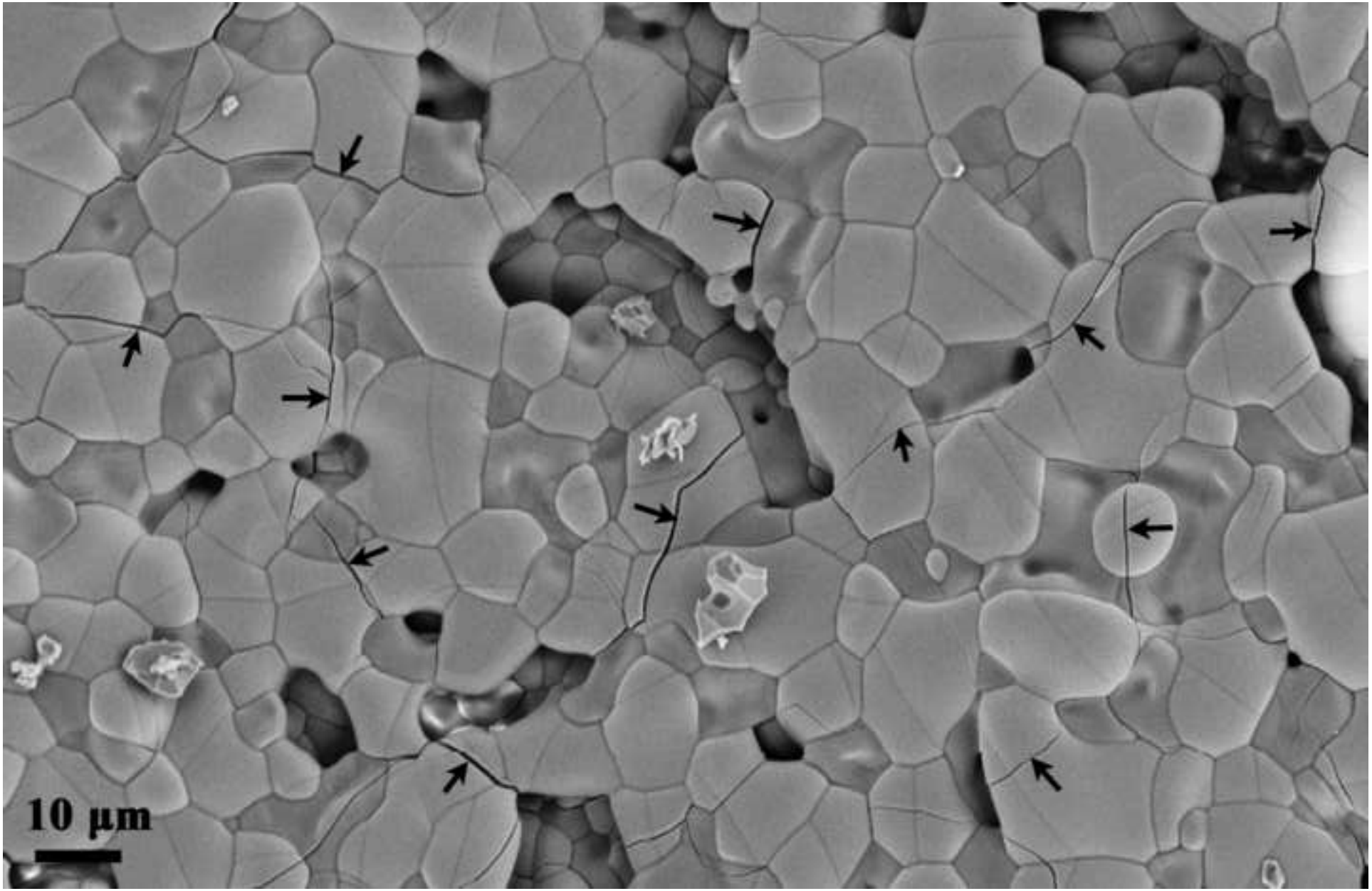

Figure 10

Click here to download high resolution image

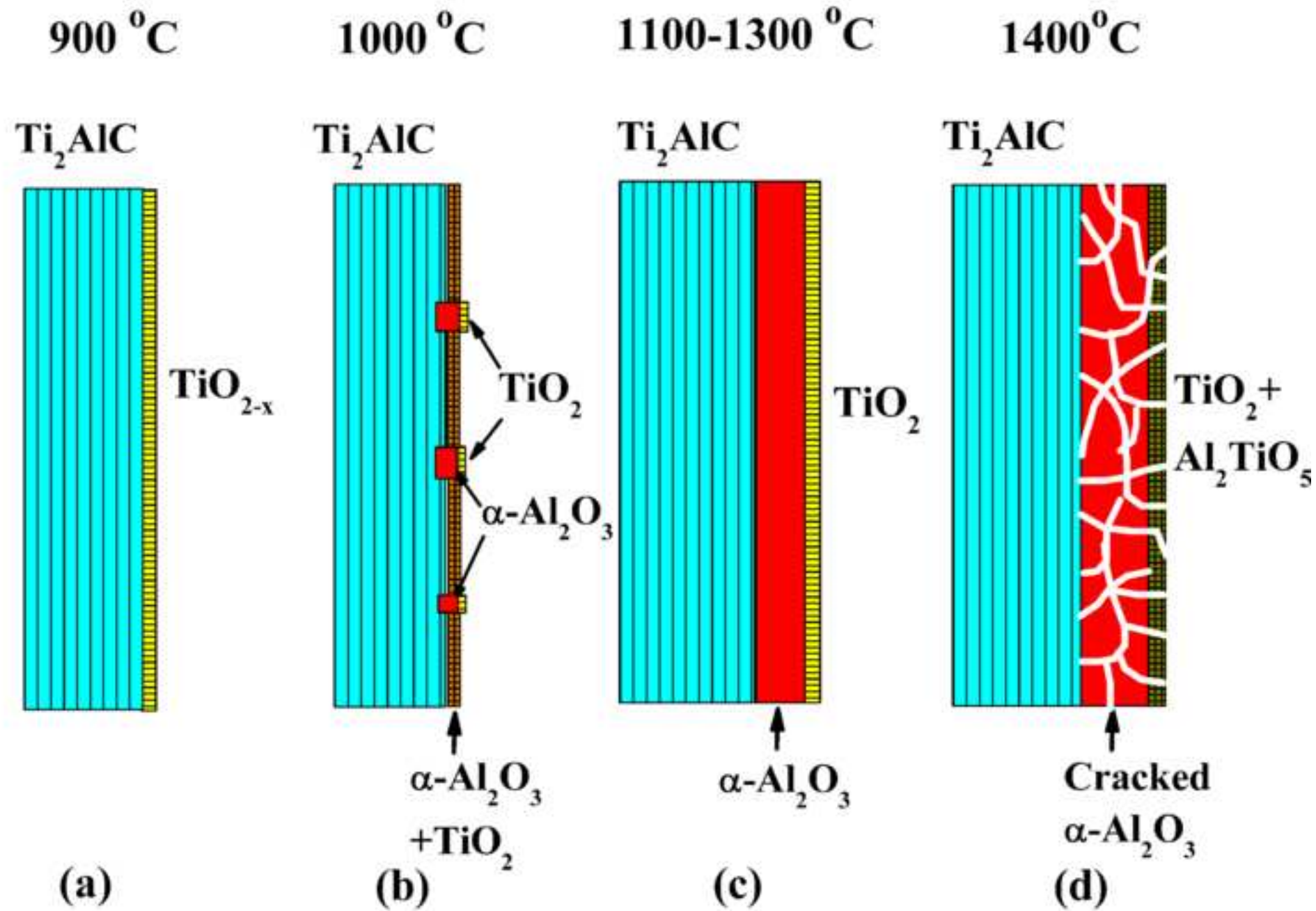

Figure 11

Click here to download high resolution image